Fragmentation Consequence Analysis for LEO and GEO Orbits

Executive Summary
Version 1.0 – July 2 2015

A.Rossi, E.M.Alessi, G.B. Valsecchi
IFAC-CNR, Italy
H.G. Lewis. A. White
University of Southampton, UK
L. Anselmo. C. Pardini
ISTI-CNR, Italy

ESA Contract No. 4000106543/12/F/MOS

Contractor Study Manager: A. Rossi (IFAC/CNR)
ESA Study Manager: H. Krag (ESA/ESOC)

Table of Contents

1. Introduction

The simulations of the long term evolution of the space debris population, under realistic assumptions, show how the driving factor in the future environment will be mostly the breakup of large spacecraft and rocket bodies in LEO.
The present distribution of intact objects is a good proxy to quantify the catastrophic collision risk and consequences in the coming decades. For this reason, it is important to understand the effects of selected ``typical" collisional fragmentations on the long term evolution of the debris population, as a function of the main driving parameters, with the goal of measuring the danger represented by ``typical" classes of space objects.
To tackle this problem, the work presented in this report presents the results of a large number of long term simulations aimed at analysing the effects on the circumterrestrial environment of many different collisional fragmentations. All the long term simulations were performed using either SDM 4.2 or DAMAGE the two well-known long term evolution codes, developed in Italy (SDM) and in the United Kingdom (DAMAGE) in the last decades.
Along with the long term numerical simulations (and based on their results), analytical models were developed to perform similar tests in a fast and reliable way.
Analytical norms and indexes were also devised to rank the fragmentation events and the in orbit objects in terms of the possible effects on the environment of the spacecraft and, conversely, in terms of the effect of the environment on the spacecraft itself.
The Contract, and this document, were structured in three main tasks:

1. Task 1 was devoted to the preliminary analysis of the environment to define the simulation plan, to analyse the past fragmentation and to assess the validity of the NASA fragmentation model. Task 1 included the following Work Packages:
    - WP 110: Review of simulation models
    - WP 120: Simulation Plan Definition
    - WP 130: LEO analytical model setup
    - WP 140: Analysis of past collisional events
2. Task 2 was devoted to the simulation work, including the validation and comparison of the used simulation models (SDM and DAMAGE) and the development of the analytical model. Task 2 included the following Work Packages:
    - WP 210: Simulation of the fragmentation target objects
    - WP 220: Long-term environment analysis
    - WP 230: Expansion of the analytical model
3. Task 3 was devoted to the analysis of the results and the ranking work. Task 3 included the following Work Packages:
    - WP 310: Impact flux assessment and analysis
    - WP 320: Criticality Evaluation and Modelling
    - WP 330: Criticality Quantification

2. The simulation planning and the review of the simulation models

A number of preliminary steps were needed to plan and optimize the Contract work.
Being a contract focused on the simulation of fragmentation events, a survey and validation of the NASA breakup model (the currently accepted *de-facto* standard in the field) was performed. Then the definition of an effective and sounding simulation plan, able to identify the main features of the orbiting targets distribution within a reasonable and manageable number of test cases to be actually simulated was performed.
After having analysed the present distribution of intact objects in orbit around the Earth and carried out a review concerning the information available on the collisions involving catalogued objects, in order to assess the need of off-centre impact simulations, analyse the energy-to-mass ratio achieved

and the corresponding fragmentation outcome, and evaluate the adequacy of the NASA standard breakup model, a detailed simulation plan for LEO and GEO is proposed, aiming at a reasonable number of cases and an optimal coverage of the situation in space, present and planned in the coming decades.
The NASA standard breakup model was found to be reasonably adequate and the total number of proposed simulation cases is 118: 94 in LEO and 24 in GEO. Moreover, it was found that, for the purposes of this study, the modelling of off-centre collisions can be disregarded.

2.1. The simulation work

All the long term simulations were performed using either SDM 4.2 or DAMAGE. They are two well-known long term evolution codes, developed in Italy (SDM) and in the United Kingdom (DAMAGE) in the last decades. The two codes allow a very detailed and accurate modeling of the debris environment in Earth orbit, taking into account all the main sources and sinks terms affecting the future evolution of the debris population. As a validation, the two models were subject to several international comparisons with similar software suites developed by other research groups and space agencies worldwide, both within the framework of the Inter-Agency Space Debris Coordination Committee (IADC) studies [13] and also in the course of the study presented here. In the following, both results obtained with SDM 4.2 and with DAMAGE will be shown alternatively, where deemed significant. The interested reader can find the whole set of plots and tables in the Final Report of this Study.
The main simulation strategy consisted in comparing the long term evolution results of a Reference scenario with those of a number of scenarios where a number of different spacecraft were supposed to collisionally fragment in selected epochs. That is, in the long term runs, at the selected epochs a given spacecraft was “artificially”' fragmented by a simulated collision and the clouds of fragments were added to the simulation. Comparing the long term evolution in the cases with and without the additional fragments generated by the artificially introduced fragmentation, the effect of the particular fragmentation on the environment was evaluated.

2.1.1. The Reference Scenario

As a reference, a long term evolution scenario was simulated for a time span of 200 years. With Reference scenario, we mean that the traffic launch repeats an 8-year cycle representing the current launch pace, that is the new launched objects are inserted into orbits similar to those populated in the recent past. An 8-year operational lifetime is assumed for future spacecraft, no new explosions are considered and no avoidance maneuvers are performed. A post mission disposal scenario according to the 25-year rule is adopted, with a 60 % compliance to this rule. That is, given all the spacecraft that do not re-enter naturally in 25 years, only 60 % of them are actually de-orbited at end-of-life. The above assumptions are common to most of the recent studies of the long term evolution of the space debris population. As in most of the modelling works, there are of course uncertainties related to these assumptions, e.g. the traffic launch cannot be predicted accurately for 200 years in the future, as well as the solar activity, etc. Nonetheless the above assumptions represent good, standard hypotheses that are well suited to produce an ``average'' reliable future environment appropriate for the purpose of the present study. The Reference scenario was simulated with 50 Monte Carlo (MC) runs both with SDM and DAMAGE and the results were compared, in order to have a reliable Reference scenario against which the fragmentations cases could be compared. In all the simulation the objects larger than 10 cm are considered. Whereas particles smaller than 10 cm can, in some peculiar cases (i.e., small targets and high impact velocities), generate catastrophic fragmentations, it was observed in previous studies that the long term collisional evolution is mainly driven by the objects larger than 10 cm that can generate large debris clouds, upon fragmentation of large targets.
Figures 1- 2 shows the main results for the Reference scenario. Figure 1 (left panel) shows the average number of objects larger than 10 cm in LEO with SDM (thick blue line) and DAMAGE (thick red line), along with the respective 1-sigma curves (thin lines). It can be noticed how the two codes give

remarkably comparable results after the long term evolution, with both averages lying well within the 1-sigma bars of the other model. This gives a clear indication that the two models can be used alternatively in the course of the study, leading to comparable and reliable results.

From the figure we can notice that the simulated scenario has a steady increasing pace with the final population nearly doubled with respect to the initial one. This is due to a significant number of collisional debris added to the environment, as shown in Figure 1 (right panel), where the green lines shows the number of intact objects as a function of time, the red lines the number of fragments already present in the environment at the 2009 initial epoch and the blue lines the fragments produced during the simulated time span. The solid lines show the results of SDM and the dashed lines the results of DAMAGE, once again showing the very good agreement between the two codes. The steady growth of the fragments shown in Figure 1 (right panel) is due to a significant number of fragmentations happening in the 200-year time span as shown in Figure 2 (left panel). In this figure the average number of fragmentations recorded by SDM (blue lines) and DAMAGE (red lines) are shown, along with their ± 1σ curves. It can be noticed how, on average, we can expect 1 collisional fragmentation every 5 years in the Reference scenario. The right panel of Figure 2 shows the altitude distribution of all the fragmentations recorded in the 50 SDM MC runs. The well-known hot spots around 800, 1000 and 1400-1500 km of altitude are clearly visible. This is a first indication that the environment in those particular regions will be heavily perturbed in the future, notwithstanding the possible additional fragmentations artificially introduced in the simulations described in the next Sections. Note that the fragmentations shown in Figure 2 all involve large targets, up to a few objects in the 8-9 tons range.

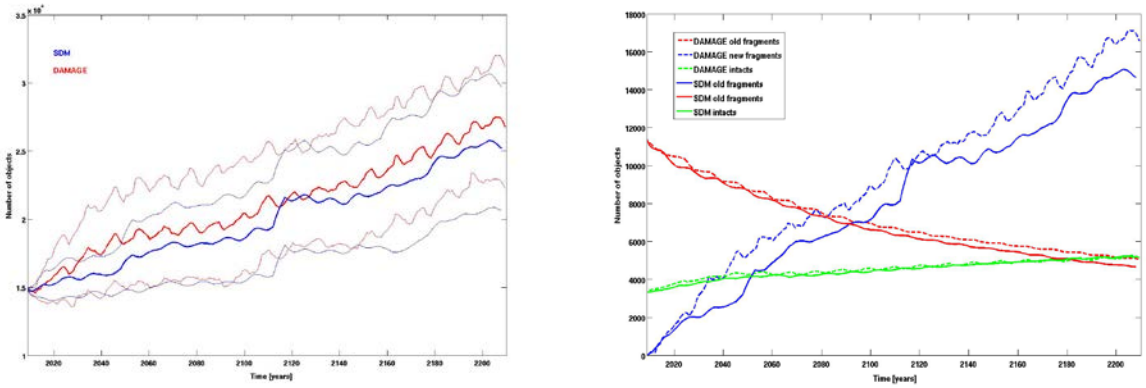

Figure 1. Left panel: Average number of objects larger than 10 cm in LEO in the Reference scenario computed with SDM (blue thick line) and DAMAGE (red thick line). The thin lines (of the corresponding colours) show the 1-sigma uncertainty intervals for both codes. Right panel: Breakdown of the population according to the type of objects: the green lines refer to the intact objects, the red line to the fragments already present in the environment at the 2009 initial epoch and the blue line shows the fragments produced during the simulated time span. The solid lines show the results of SDM while the dashed lines show the results of DAMAGE.

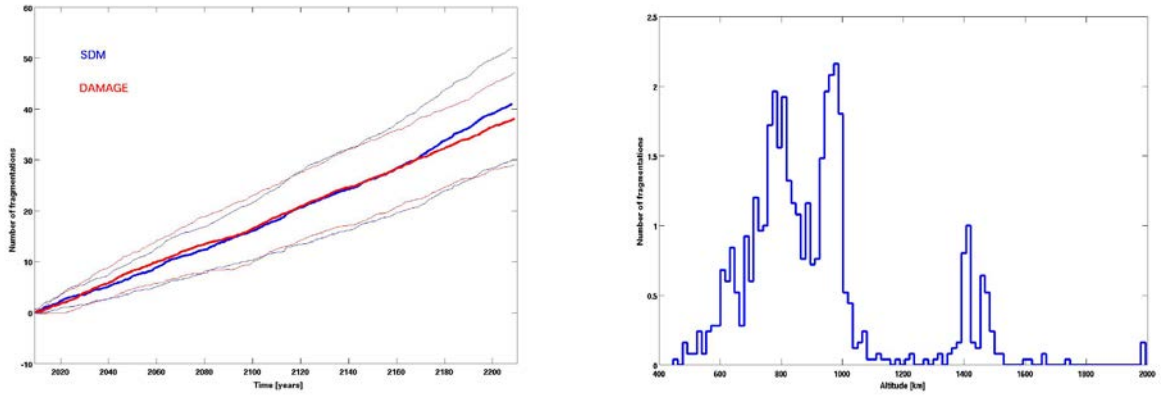

Figure 2. Left panel: Average number of fragmentations in the Reference scenario. The thick blue line shows the average number of events in the SDM simulations while the thick red line shows the similar results from DAMAGE. The thin lines show the 1-sigma uncertainties. Right panel: Altitude distribution of the fragmentations recorded in the SDM simulations of the Reference scenario in LEO

2.1.2. The LEO fragmentations

A total of 46 fragmentations happening in LEO were simulated. The selected location and the nature of the targets fragmented reflects the actual distribution of the intact objects currently in orbit. As mentioned in Sec. 2.1, a thorough analysis, parametrizing the objects in terms of orbital elements and mass bins, was preliminary conducted to identify the most prominent and representative target objects, identifying a total of 112 orbit-mass bins representing the hot spots of intact object distribution in LEO. A number of filters on size, mass and orbital elements was applied to reduce the number of representative targets. In particular, the cases, in LEO, with inclinations lower than 50 degrees (a part from the Ariane upper stages) and the objects with mass lower than 500 kg (with the exception of the Globalstar spacecraft, filling a specific gap in the orbital bin distribution) were excluded. Moreover a coarser resolution in the mass spectra (e.g., merging the bins involving objects with masses differing by less than 30 %) was finally adopted. As a result of this analysis, Table 1 lists the first 45 fragmentation events simulated in LEO. All the scenarios of Table 1 were simulated with 25 MC runs and the scenarios were repeated twice: one with the fragmentation happening in the year 2020 and another one with the event happening in 2070.

Moreover, since one of the drivers of the present study was the concern for the consequences on the environment of a possible future fragmentation of Envisat, beyond all the events of Table 1, the fragmentation of Envisat was also analyzed with particular care. As it is known, after 10 years of fruitful Earth observations, the contacts with the large spacecraft were lost on 8 April 2012 and ESA formally announced the end of Envisat's mission on 9 May 2012. The mass of Envisat is around 8 tons and it is still orbiting in the very crowded region around 750 km of altitude. Due to its altitude, the residual lifetime in orbit is estimated in excess of 100 years. Therefore, there is a significant risk that Envisat could be fragmented upon impact with a debris in the future, creating a large debris cloud. For these reasons a particular set of simulations was devoted to the study of the Envisat case. It was decided to simulate the fragmentation of an Envisat-like spacecraft at four different epochs in the future: in the year 2020, 2045, 2070 and 2095. The fragmentations are simulated along the decaying orbit, that is the orbit of Envisat is propagated for its residual lifetime and each fragmentation is happening at the altitude reached by the spacecraft at the desired epoch. **Table 2** shows the orbital elements used. The spacecraft mass was assumed to be, in all the epochs, equal to 8050 kg and the fragmentation simulated was due to an impact against a projectile of 6.44 kg travelling at 10 km/sec. 50 MC runs were performed for each scenario.

#	Project. Mass [kg]	Target Mass [kg]	Inc. [deg]	a [km]	Ecc.	RAAN [deg]	Arg. Of perigee [deg]	True Anom [deg]	Altitude [km]	Type
1	1.440	1800	7.0	22468	0.7036	270.0	205.0	34.4	800	Ariane 4 R/B in GTO
2	2.880	3600	5.0	24445	0.7167	100.0	200.0	23.7	801	Ariane 5 R/B in GTO
3	0.280	350	52.0	7792	0.0003	252.0	8.0	90.0	1414	Globalstar (operational)
4	1.120	1400	56.1	7813	0.0096	113.0	319.0	90.6	1435	Cosmos-3M R/B (2nd St)
5	1.200	1500	63.1	26574	0.7334	0.0	280.0	14.2	800	Molniya
6	1.040	1300	65.0	7343	0.0030	60.0	74.0	90.2	965	US-A (RORSAT)
7	1.000	1250	65.0	26563	0.7034	0.0	270.0	0.0	1500	US-K Oko
8	0.760	950	65.8	7335	0.0012	35.0	73.0	90.1	957	DS-P1-M (Lira)
9	1.120	1400	65.8	7354	0.0063	63.0	270.0	90.4	976	Cosmos-3M R/B (2nd St)
10	2.600	3250	71.0	7230	0.0008	151.0	167.0	95.3	852	Tselina-2
11	6.640	8300	71.0	7222	0.0014	254.0	0.0	90.1	844	Zenit-2 R/B (2nd St)
12	1.200	1500	73.6	7881	0.0029	223.0	139.0	91.4	1503	GEO-IK (Musson)
13	0.720	900	74.0	7170	0.0015	29.0	58.0	90.1	792	Strela-2M
14	1.120	1400	74.0	7149	0.0017	4.0	277.0	90.1	771	Cosmos-3M R/B (2nd St)
15	0.640	800	74.0	7357	0.0023	164.0	78.0	90.1	979	Tsiklon
16	1.120	1400	74.0	7363	0.0020	224.0	139.0	90.1	985	Cosmos-3M R/B (2nd St)
17	0.480	600	74.0	7772	0.0039	67.0	335.0	90.1	1394	Sfera
18	1.120	1400	74.0	7567	0.0034	131.0	23.0	90.1	1189	Cosmos-3M R/B (2nd St)
19	1.120	1400	74.0	7964	0.0133	123.0	236.0	90.8	1586	Cosmos-3M R/B (2nd St)
20	1.400	1750	81.2	6979	0.0014	320.0	198.0	90.1	601	Tselina-D
21	3.040	3800	81.2	7246	0.0039	302.0	63.0	90.1	868	Meteor-1
22	2.200	2750	81.2	7237	0.0025	341.0	98.0	90.1	859	Meteor-2
23	1.072	1340	81.2	7231	0.0089	92.0	87.0	90.5	853	Vostok R/B
24	2.200	2750	82.5	7326	0.0016	199.0	112.0	90.1	948	Meteor-2
25	1.128	1410	82.5	7326	0.0014	31.0	309.0	90.1	948	Tsiklon-3 R/B
26	1.720	2150	82.5	7574	0.0018	187.0	170.0	90.1	1196	Meteor-3
27	1.128	1410	82.5	7614	0.0016	31.0	262.0	90.1	1236	Tsiklon-3 R/B
28	1.128	1410	82.5	7874	0.0008	215.0	169.0	90.1	1496	Tsiklon-3 R/B
29	0.640	800	83.0	7355	0.0026	45.0	356.0	90.1	977	Tsiklon
30	1.120	1400	83.0	7347	0.0042	344.0	143.0	90.1	969	Cosmos-3M R/B (2nd St)
31	0.480	600	83.0	7563	0.0036	250.0	339.0	90.1	1185	Sfera
32	1.120	1400	83.0	7568	0.0053	282.0	88.0	90.3	1190	Cosmos-3M R/B (2nd St)
33	0.560	700	86.4	7156	0.0003	328.0	78.0	90.0	778	Iridium (operational)
34	0.480	600	90.0	7442	0.0056	320.0	306.0	90.3	1064	Able-Star R/B
35	0.800	1000	98.0	7057	0.0009	112.0	212.0	90.1	679	GeoEye-1 in SSO
36	1.600	2000	98.0	7001	0.0001	223.0	76.0	90.1	623	COSMO-Skymed (in SSO)
37	3.200	4000	98.0	7053	0.0001	113.0	163.0	90.1	675	Helios-2 in SSO
38	6.400	8000	98.0	7017	0.0016	359.0	179.0	90.1	639	Zenit-2 R/B (2nd St) (in SSO)
39	0.800	1000	98.5	7119	0.0143	291.0	307.0	90.8	741	Delta 2 R/B in SSO
40	1.600	2000	98.5	7147	0.0011	21.0	43.0	90.1	769	Ariane 4 R/B in SSO
41	3.200	4000	98.5	7158	0.0014	9.0	274.0	90.1	780	SSO S/C & R/B
42	0.800	1000	99.0	7233	0.0015	339.0	83.0	90.1	855	NOAA-19 in SSO
43	1.600	2000	99.0	7276	0.0014	16.0	118.0	90.1	898	SSO S/C & R/B
44	3.200	4000	99.0	7276	0.0014	90.0	156.0	90.1	898	SSO S/C & R/B
45	6.400	8000	99.0	7375	0.0016	222.0	153.0	90.1	997	Zenit-2 R/B (2nd St) (in SSO)

Table 1. List of all the simulated LEO fragmentations. The events listed in blue were simulated with SDM, those in red were simulated with DAMAGE.

Epoch	Semimajor axis [km]	Eccentricity	Inclination [deg]
2020	7137	0.0011	98.2
2045	7121	0.0001	98.4
2070	7099	0.0001	98.6
2095	7073	0.0013	98.4

Table 2. Orbital elements of the fragmented Envisat-like spacecraft

2.1.2.1 The Envisat results

The left panel of Figure 3 shows the average number of objects in LEO larger than 10 cm, as a function of time, computed with SDM in 4 different scenarios: the thick blue line shows the Reference scenario results (as in Figure 1, thick blue line), the red line shows the number of objects in the case where the fragmentation of the Envisat-like spacecraft is happening in the year 2020, the magenta line shows the results for the fragmentation happening in the year 2070 and the black line shows the results for the fragmentation happening in the year 2095. The thin blue lines are the ± 1σ curves for the Reference scenario. The right panel of Figure 3 shows the average number of fragmentations happening in the Envisat scenarios, again compared with the Reference one. It can be noticed how the average number of fragmentations is around 40 over 200 years, with no significant deviations between the Reference and the Envisat fragmentation scenarios.

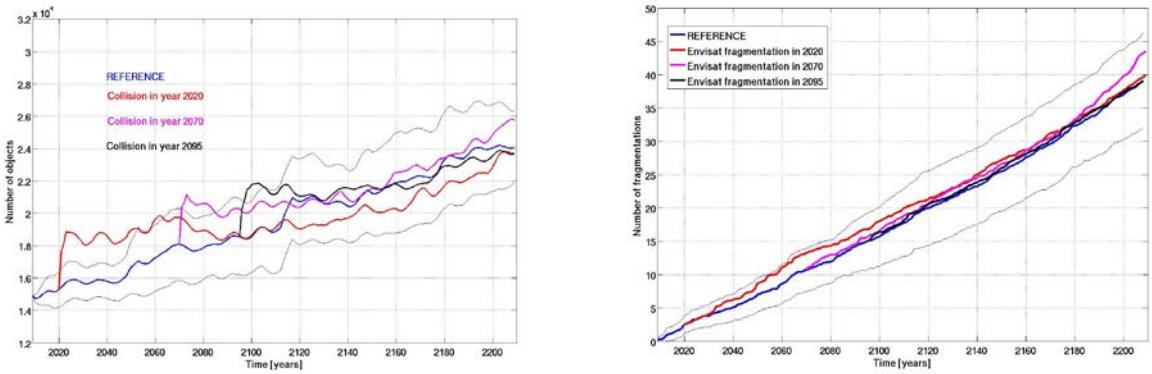

Figure 3. Left panel: Comparison between the average number of objects larger than 10 cm in LEO in the Reference scenario (thick blue line) with the scenarios where the fragmentation of an Envisat-like spacecraft is simulated in the year 2020 (red line), 2070 (magenta line) and 2095 (black line). The thin blue lines show the ± 1σ interval for the Reference scenario. Right panel: Cumulative number of collisions in the scenarios described in the left panel.

Contrary to what one might expect, the final number of objects in all the four cases is statistically the same (i.e., all well within the ± 1σ standard deviation bounds). From a statistical point of view, the Envisat fragmentations are leading to a long term LEO environment which is indistinguishable from the Reference one. This means that, in the long run, even the fragmentation of a very large spacecraft leaves no noticeable signature on the environment or, in other words, the simulated Envisat fragmentation does not alter, by itself, "permanently'" the LEO environment on the long run (200 years). The reason for this outcome is that the reference evolution is highly stochastic and is dominated by a large number of fragmentations (on average one every 5 years).
Therefore, the effects of our additional Envisat-like fragmentation get soon "diluted" in the vast number of background fragments and leave almost no trace after 200 years. On the other hand, the situation can be different in the "interim" regime, in the orbital regions in the vicinity of the Envisat fragmentation, during the few decades following the event; these shorter term effects have been studied too and will be described later. Note that the same scenarios described in Figure 3 were simulated with DAMAGE. The results are again perfectly comparable and are therefore not shown here for sake of conciseness.

2.1.2.2 Results of the LEO cases

As mentioned above, the full set of results can be found in the Final Report of the Contract. Here, due to lack of space it is impossible to show the results for all the fragmentations listed in Table 1. Only some representative results will be therefore displayed and the interested reader can refer to Final Report for the complete set of plots. Figure 4 shows the comparison between the average number of objects in LEO in the Reference scenario and for three different scenarios where an 8 ton Zenit-2 R/B

in Sun Synchronous Orbit (SSO) is fragmented in the year 2020. In particular, as usual, in the picture, the blue lines refer to the Reference scenario. Then the black line refers to the scenario where the fragmentation happens at an altitude of 639 km, the magenta line to the fragmentation at an altitude of 844 km and, finally, the red line to the fragmentation at 997 km.
A first consideration can be made looking at Figure 4 and Figure 5 in none of the cases (and this is true also for the other scenarios not shown here; see the Final Report) the average number of objects in the fragmentation cases, at the end of the investigated time span, lies outside the ± 1σ intervals of the Reference scenario. This means that, statistically speaking, all the events of Table 1 are leading to a long term LEO environment which is indistinguishable from the Reference one. In other words, even a large fragmentation on a high LEO is not leaving a strong statistically significant long term signature on the environment. On the other hand, it has to be stressed that this outcome is also related to the large span covered by the ± 1σ curves, which in turns is related to the number of MC runs. Since the ± 1σ curves represent formal uncertainties out of the MC averaging process, the value of σ is decreasing as the square root of the number of runs. That is, while the displayed results give a reliable statistical indication of the long term evolution, performing a significantly larger number of runs we could limit the ± 1σ intervals and therefore obtain results more sounding from the statistical point of view. Of course, with the large number of simulations foreseen in this study it would have been impossible to increase the number of MC runs to reach this higher level of significance.

Notwithstanding the mentioned caveats, as it will be detailed in the following, some events show long term consequences which can be clearly spotted in the plots and that highlight the driving factors in the environment evolution, which is the main expected output of this study. The first parameter of interest in the simulation is the mass. Again a general consideration can be made here: whenever the mass of the fragmented target is lower than about 1000 kg, no appreciable signature is left on the environment. That is, as stated above even for the much more massive Envisat cases, these kind of events get soon lost in the sea of fragments generated by the other fragmentations.

The largest objects listed in Table 1 are the Zenit rocket bodies of cases 11, 38 and 45, with a mass of 8 tons. Looking at Figure 4 it can be noticed how the consequences of the year 2020 fragmentations are visible in the long term environment of cases 11 and 45, while no signature of the 2020 fragmentation is left in case 38. These differences are clearly related to the altitude of the event. Whereas the fragmentations 11 and 45 happens at high altitudes, respectively at 844 and 997 km, the event number 38 happens more than 200 km below, at 639 km of altitude. The lifetime of the fragments is therefore significantly reduced. These first considerations already point us to the interplay of the most important parameters driving the evolution: mass and altitude. This is also noticeable looking at Figure 5. In this picture the final evolution is comparable in the three cases, with the lowest altitude one (case 36) being slightly lower than the other two. Moreover it can be seen how the effects of the cloud generated in case 36 “expires” much faster than in the other two cases, due to the significantly higher atmospheric drag present around 600 km.
As an example of the interplay between mass and altitude and of the complexity and stochasticity of the problem one can look at Figure 6, showing the results of the fragmentation of Cosmos-3M R/B on different circular LEO orbits at 771 (red line, fragmentation number 14), 985 (magenta line, fragmentation number 16), 1189 (black line, fragmentation number 18) and 1589 km (green line, fragmentation number 19) of altitude, respectively. In the first case, with the event happening at 771 km, the Reference and fragmentation scenarios become nearly coincident just a few decades after the collision. This is due to the cleansing effect of the drag on the relatively small debris cloud produced by the moderate mass of the target. A different pattern is noticeable in the magenta line, where the long term evolution of the Reference and fragmentation scenarios follow two parallel and clearly separated tracks, with the signature of the fragmentation apparently visible even after 200 years. This behaviour is clearly dictated by the more than 200 km of difference in altitude with the previous case. Moreover, it is worth noticing that the fragmentation number 16 is happening at the altitude of 980

km, right in the middle of one of the most crowded LEO zone, therefore it is plausible that the added perturbation could generate feedback collisions in the years following the event. Therefore these two events seem to confirm the above conclusions on the role of mass and altitude. Then, the black line shows a similar situation, even if here the onset of the separate track for the fragmentation case appears to be happening only about 40 years after the collision and could be ascribed to other collisions in the region, possibly, but not necessarily, triggered by the perturbed environment produced by the 2020 fragmentation. Also this event, at 1189 km of altitude, is happening close to the densely populated area around 900 km of altitude, so its debris cloud would be interacting in the decades after the event, with a large number of other potential targets. The apparently clear picture just described above is complicated by the results shown by the case of fragmentation number 19 (green line). Here the same mass is fragmented on a significantly higher orbit, but the red and blue lines are almost indistinguishable. A possible explanation here is that, while higher, the event is happening in a much less populated zone so that subsequent feedback collisions are less likely to occur.

These latter results point out another important actor in this story, that is the region where the fragmentation takes place, namely in the sense of the spatial density of objects with which the fragments cloud will be interacting. Figure 7, similarly to Figure 6 shows again the average number of objects larger than 10 cm for several scenarios involving the fragmentation of targets with a mass of about 1400 kg, namely the cases 9, 14, 16, 18, 19, 25, 27, 30 and 32. Apart from the Reference scenario (in blue), in this plot all the fragmentation cases are shown with the red lines, except for case 14 (black line), which represents, within the 9 cases considered in the figure, the fragmentation happening on the lowest orbit (at an altitude of 770 km), and case 19 (green line), which represents the fragmentation happening on the highest orbit (at an altitude of 1580). Note that all the cases shown with the red lines refer to fragmentations happening between 950 and 1450 km of altitude, that is on orbits with long residual lifetime. Looking at the plot, it can be noticed how the black line, representing an event happening about 200 km below anyone else, indeed is one of the lowest (but it is not the lowest one). Moreover, clearly all the other cases are either above or below the Reference one, without a clear separation related to the altitude of the event and, in particular, the green line is not on the top of the group. It might be argued that above about 900 km, where the average residual lifetime of the fragments exceeds the investigated time span, the effects of the altitude of the fragmentation, while more important in absolute terms, become less strong as a ranking factor (i.e., it becomes more difficult to anticipate the consequences of an event with respect to a similar one on a different orbit on the basis of their altitude). For sake of completeness, it can be added that the three top red line lines, above the Reference line, refer to the cases 16, 18 and 25, happening between 950 and 1190 km of altitude, whereas the bottom red line pertains to the case 9, happening at about 980 km of altitude. The only significant difference between the orbits of the targets of case 9 and cases 16, 18 and 25, is that the target of case 9 is on a slightly less inclined orbit, at 65.8 deg, whereas, e.g., the target of case 16 (at nearly the same altitude) is on an orbit with 74 deg of inclination. Although far from conclusive, this might draw our attention to the influence of the inclination on the long term consequences of a fragmentation in LEO. As it is well known, a cloud of debris with near polar inclination will interact with all the orbits in the region, with dangerous crossings close to the poles, thus increasing the overall collision risk.

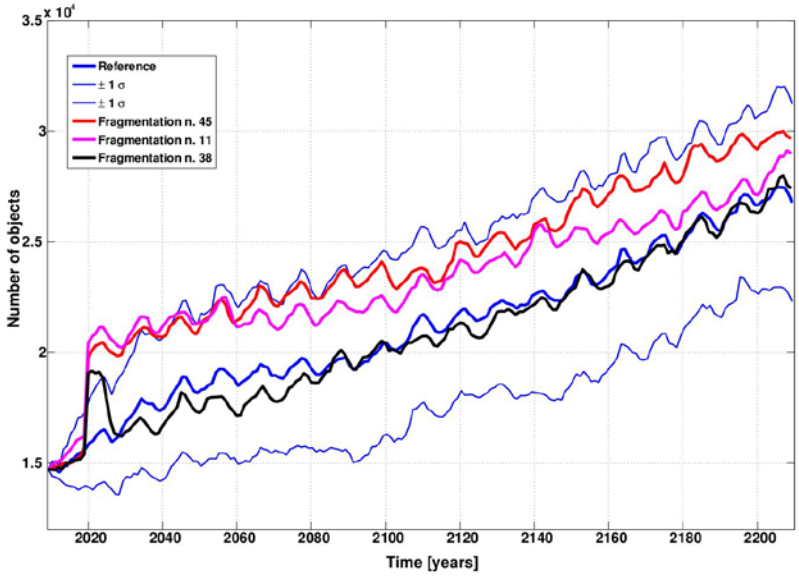

Figure 4. Average number of objects larger than 10 cm in LEO for the fragmentations number 11, 38 and 45, all involving targets of about 8000 kg of mass. The thick blue line shows the Reference scenario and the thin blue lines show the ± 1σ interval for the Reference scenario. The black line shows the evolution for the case of fragmentation number 38 (happening at an altitude of about 639 km), the magenta line for the case 11 (844 km of altitude) and the red line for the case 45 (997 km of altitude).

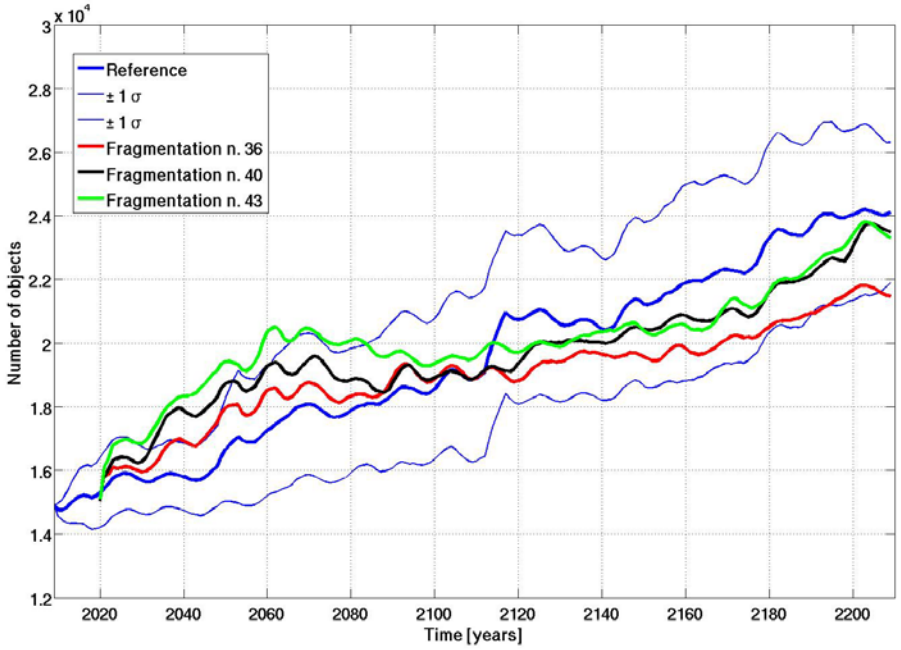

Figure 5. Average number of objects larger than 10 cm in LEO for the fragmentations number 36, 40 and 43, all involving targets of 2000 kg of mass. The thick blue line shows the Reference scenario and the thin blue lines show the ± 1σ interval for the Reference scenario. The red line shows the evolution for the case of fragmentation number 36 (happening at an altitude of about 620 km), the black line for the case 40 (769 km of altitude) and the green line for the case 43 (900 km of altitude).

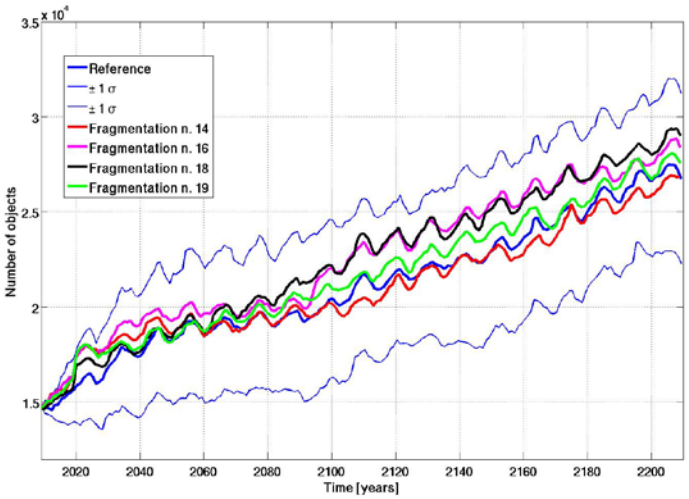

Figure 6. Average number of objects larger than 10 cm in LEO for the fragmentations number 14, 16, 18 and 19, all involving Cosmos R/B of about 1400 kg of mass. The thick blue line shows the Reference scenario and the thin blue lines show the ± 1σ interval for the Reference scenario. The red line shows the evolution for the case of fragmentation number 14 (at an altitude of 771 km), the magenta line refers to the fragmentation number 16 (altitude: 985 km), the black line to the fragmentation number 18 (altitude: 1189 km) and the green line to the fragmentation number 19 (altitude: 1586 km).

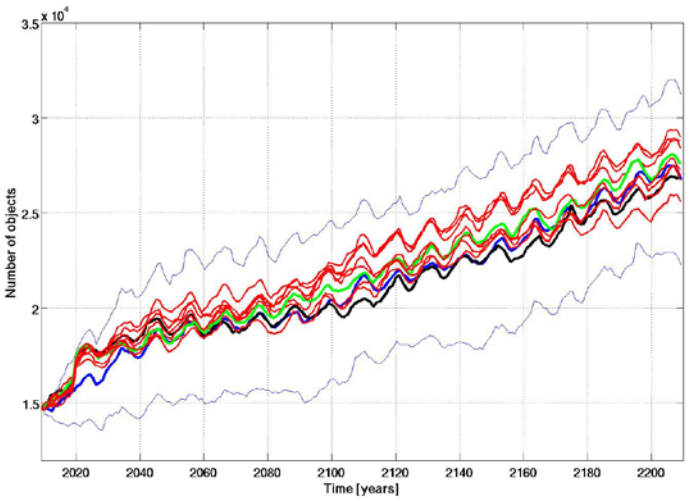

Figure 7. Average number of objects larger than 10 cm in LEO for the fragmentations number 9, 14, 16, 18, 19, 25, 27, 30 and 32, all involving targets of about 1400 kg of mass. The thick blue line shows the Reference scenario and the thin blue lines show the ± 1σ interval for the Reference scenario. The black line shows the evolution for the case of fragmentation number 14 (having the lowest orbit in the selected group, with an altitude of about 770 km) and the green line shows the evolution for the case number 19 (having the highest orbit in the selected group, with an altitude of about 1580 km). All the other cases are shown with red lines, happening in orbits ranging from 950 to 1450 km of altitude.

2.1.2.3 The Criticality evaluation norm

In order to properly analyse and highlight the effects of the additional fragmentation events with respect to the underlying reference environment an evaluation norm was introduced. The norm also helps to quantify and easily visualize the results of the simulations. The definition of the norm is as follows.

Given the underlying "Reference" scenario, described in Sec. 2.1.1, and a "fragmentation" scenario in which the simulation of a particular fragmentation is added, the number of objects as a function of time, averaged over all the MC runs is computed for both scenarios. Let $n_{REF}(i)$ be the average number

of objects in the Reference scenario and $n_{FRAG}(i)$ the average number of objects in the fragmentation case, in the i-th year. Then, the growth of the population of the ``fragmentation" scenario w.r.t. the ``Reference" one can be quantified by:

$$C_i = \left(\frac{n_{FRAG}(i) - n_{REF}(i)}{\sigma_{REF}(i)} \right),$$

if $(n_{FRAG}(i) - n_{REF}(i)) \geq 0$ else $C_i = 0$. σ_{REF} is the standard deviation of the reference Monte Carlo runs. Whenever $C_i > 1$ the environment is perturbed by the fragmentation event to a level that is above the statistical "noise" of the MC method. From the values of a C_i a ranking of the danger represented by selected fragmentations can be easily expressed with a single number, called C*. In fact, the sum of the differences, weighted by the time interval, gives an indication of the criticality:

$$C^* = \sum_{i=1}^{N} \frac{C_i}{N} = \sum_{i=1}^{N} \left(\frac{n_{FRAG}(i) - n_{REF}(i)}{\sigma_{REF}(i)} \right) /N,$$

if $(n_{FRAG}(i) - n_{REF}(i)) \geq 0$ else $C_i = 0$. N is the number of years in the simulation.
As an example, Figure 8 plots the value of C_i in the case of the Envisat fragmentation scenarios shown in Figure 3. The decreasing relative importance of the fragmentations happening in later years (due to the larger number of background fragments, to the increase of the value of $\sigma_{REF}(i)$ as a function of time and, mainly, to the lower altitude of the event) is clearly highlighted here.

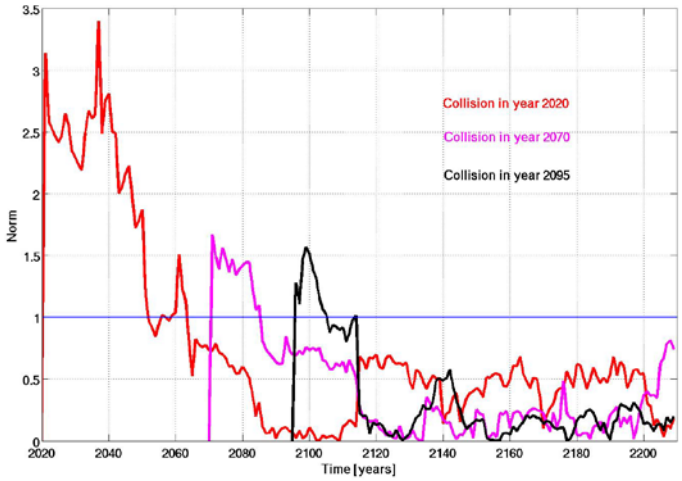

Figure 8. The time evolution of the norm, computed for the three Envisat-like fragmentations, shown in Figure 3.

A classification of all the fragmentation events simulated can be performed using the criticality evaluation norm, C*.
Note that the two sets of simulations (SDM and DAMAGE) had to be kept separated since the computation of C* depends on the value of the standard deviation, $\sigma_{REF}(i)$, of the Monte Carlo process, so each model must be processed coherently with its own $\sigma_{REF}(i)$. That is, being model dependent, the C* values have to be considered as relative evaluations of the effect of a given fragmentation within each model.
The relation between the C* and the physical and orbital parameters of the fragmented objects can be plotted to highlight the main factors driving the long term evolution.
In particular the plots in Figure 9 show the relation between the C* values and the mass and altitude of the fragmented objects for the cases simulated with SDM. The results are fitted with a simple linear

relation of the form: f(x)=ax+b. The linear fit clearly visualizes the growing trend as a function of mass and altitude of the target. It can be noticed how the data are quite dispersed around the linear fit (and this is reflected in the classical indicator of the goodness of the fit, such as the summed square of residuals, the sum of squares of the regression, etc). In particular, the relation with the inclination (not shown here) is poorer than with the other two parameters. Beyond the variability mentioned above, this is related to the fact that, as already mentioned, it is actually a combination of the different parameters that drives the evolution. In fact the situation improves significantly if the fit is attempted for a plot where the relation between a linear combination of the parameters and the C* is considered. In particular, Figure 10 shows the relation between C* and the product of the altitude of the fragmentation by the mass of the target (normalized to 10000 kg for ease of visualization) and by a function of the inclination, Γ=[(1-\cos(i))/2].

In this case the linear fit still shows a trend similar to that of Figure 12, but with significantly better (almost doubled) goodness indicators. It is worth noting that the addition of the inclination function Γ to the fit does not improve the level of the fit, giving a further indication that, on the long term, the initial inclination of the target is playing a minor role.

The DAMAGE plots show similar results and are not included since they are not adding significant information to what was described above.

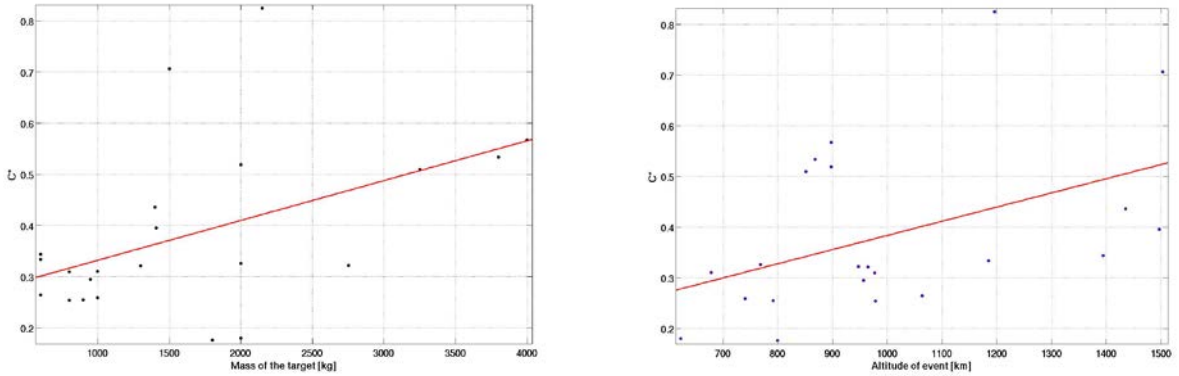

Figure 9. Linear fit of the C* values as a function of the mass (left panel) and altitude (right panel) of the fragmentation, for the cases simulated with SDM.

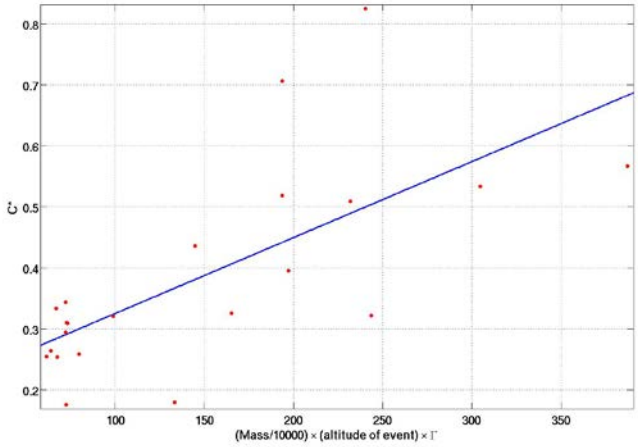

Figure 10. Linear fit of the C values as a function of the mass of the target (normalized to 10000 kg) multiplied by the altitude of the fragmentation and the inclination function Γ (see text for details), for the cases simulated with SDM.

2.1.2.4 LEO cases: short term analysis

In the previous sections the focus was on the long term effects of a given fragmentation. As already mentioned, only a few specific events leave a significant signature on the long term evolution of the overall population. This, of course, does not mean that the simulated fragmentations have no consequences on the environment and in particular on the orbital zone around the altitude of the event. That is, in the transient period before the fragments coming from the forced fragmentation, get "absorbed" by the background fragments produced by other collisions, the spatial density of objects in the vicinity of the orbit of the target is significantly increased, thus leading to possible feedback collisions and, certainly, to dangerous crossings with the operational spacecraft in that region. As an example, Figures 11 - 12 show the spatial density of objects as a function of time, around the altitude of the fragmentation, for three events from Table 1. The left panel of Figure 11 shows the time evolution of the spatial density of objects larger than 10 cm in the altitude shell between 900 and 1000 km, for the case number 24 in Table 1, namely a Meteor-2 spacecraft with a mass of 2750 kg, fragmented in the year 2020 at an altitude of 948 km. The right panel of Figure 11 is instead showing the same quantity, in the altitude shell between 850 and 950 km of altitude, for the case number 44 in Table 1, namely a Sun Synchronous spacecraft with a mass of 4000 kg, fragmented in the year 2020 at an altitude of 898 km.

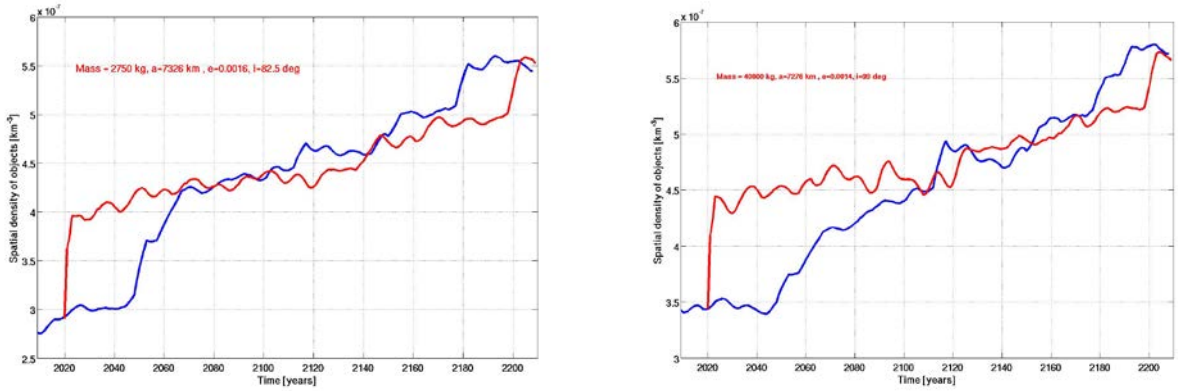

Figure 11. Left panel: spatial density of objects larger than 10 cm as a function of time for the fragmentation number 24 (red line) with respect to the Reference scenario (blue line). Right panel: the same quantity as in the left panel, for the fragmentation number 44.

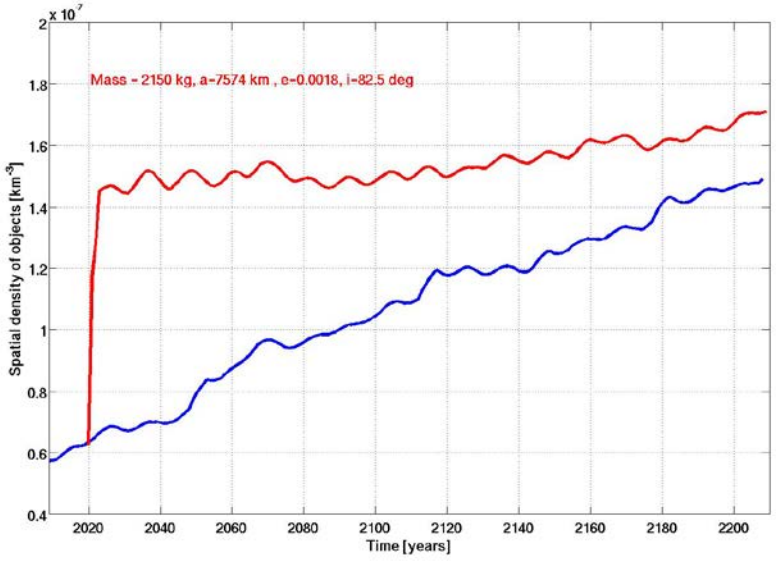

Figure 12. Spatial density of objects larger than 10 cm as a function of time for the fragmentation number 26 (red line) with respect to the Reference scenario (blue line).

Figure 12 shows the same quantity, in the altitude shell between 1150 and 1250 km of altitude, for the case number 26 in Table 1, namely a Meteor 3 spacecraft with a mass of 2150 kg, fragmented in the year 2020 at an altitude of 1196 km.
Looking at the plots it is clear how in the highest shell the density remains actually significantly above the reference level throughout the simulation time span, due to the added fragmentation of the large Meteor-3 spacecraft. Lowering the altitude of the event, in Figure 11, it can be noticed how the "local" environment in the vicinity of the target orbits still remains highly perturbed for a timespan between 40 to 80 years. This analysis of the short term effects highlights the fact that, even if it might be inconsequential on the overall long term evolution of the whole LEO environment, a massive fragmentation perturbs the local situation around the original target orbit thus jeopardizing all the spacecraft orbiting in that region. Further analysis of the local short term consequences of the simulated fragmentations would certainly deserve additional efforts in the future.

2.1.3. The GEO fragmentations

Table 3 summarizes the fragmentation events simulated in GEO.
For each one of the events in the list, a scenario with the fragmentation happening in the year 2020 and a scenario with the fragmentation happening in the year 2070 were simulated. For each scenario 25 MC runs were performed.
In this section we will summarize the results of the simulations, concentrating on the most significant events. In the following we will refer to each event with the identification number listed in the first column of Table 3. Figure 13 show the average effective number of objects larger than 10 cm in the GEO region for some of the scenarios of Table 3. The thick blue line shows the number of objects in the Reference scenario, described in Sec 2.1.1, while the thin blue lines show the ± 1 σ intervals of the MC runs of the Reference scenario. The left panel of Figure 13 shows the comparison between the Reference scenario and the cases where a 1000 kg spacecraft is fragmented in the year 2020 on an operational orbit (case number 1, red line), in an inclined orbit at the GEO altitude (abandoned object of case 5, magenta line) and in an inclined graveyard orbit (case 11, black line). Similarly, the right panel of Figure 16 shows the comparison between the Reference scenario and the cases where a 3000 kg spacecraft is fragmented in the year 2020 on an operational orbit (case number 2, red line), in an inclined orbit at the GEO altitude (abandoned object of case 6, magenta line) and in an inclined graveyard orbit (case 12, black line).
As an example of the influence of the epoch of the fragmentation, the right panel of Figure 13 shows the comparison between the Reference scenario (blue line) and the cases where a 3000 kg spacecraft is fragmented, in a GEO graveyard orbit with an equatorial inclination of 7.5 degrees (case 10 of Table 3), either in the year 2020 (red line) or in the 2070 (black line).
As a general comment, it can be noticed how the situation appears clearly different here with respect to the LEO cases. Due to the lower background population and to the lower number of fragmentation events in the Reference scenario, a massive collisional fragmentation, either in the year 2020 or 2070, is altering the GEO environment indefinitely. On the other hand, it should be noted that, in all the cases involving a fragmentation of a 1000 kg spacecraft, the evolution remains well within the ± 1 σ intervals of the Reference scenario. In fact, also in all the 50 MC runs of the Reference, on average, about 1.5 fragmentations (involving a large target between 2000 and 6000 kg of mass) are happening in the investigated GEO region. In the cases where the fragmentation of a 3000 kg spacecraft is simulated, the long term evolution of the fragmentation cases of Table 3 lies at the upper border of the ± 1 σ curve, but still mostly below it.
It is worth stressing that in the long term evolution no relation with the initial orbit of the target (i.e., altitude above the GEO ring and inclination) is detectable. That is, for the GEO cases, the driving factor seems to be just the target mass. Moreover, moving the epoch of the event from 2020 to 2070 does not change the overall characteristics of the long term evolution.

#	Project. Mass [kg]	Target Mass [kg]	Inc. [deg]	a [km]	Ecc.	RAAN [deg]	Arg. Of perigee [deg]	True Anom [deg]	Altitude [km]	Type
1	125.0	1000	0.1	42164	0.0005	85.0	235.0	125.0	35798	GEO S/C (operational)
2	375.0	3000	0.1	42164	0.0005	265.0	64.0	296.0	35777	GEO S/C (operational)
3	125.0	1000	7.5	42164	0.0030	56.0	288.0	72.0	35746	GEO S/C (abandoned)
4	375.0	3000	7.5	42164	0.0030	310.0	23.0	337.0	35669	GEO S/C (abandoned)
5	125.0	1000	15.0	42164	0.0030	0.0	90.0	270.0	35785	GEO S/C (abandoned)
6	375.0	3000	15.0	42164	0.0030	0.0	270.0	90.0	35785	GEO S/C (abandoned)
7	125.0	1000	0.1	42600	0.0030	265.0	49.0	311.0	36138	GEO S/C (reorbited)
8	375.0	3000	0.1	42600	0.0030	85.0	200.0	160.0	36342	GEO S/C (reorbited)
9	125.0	1000	7.5	42600	0.0030	310.0	290.0	70.0	36178	GEO S/C (reorbited)
10	375.0	3000	7.5	42600	0.0030	56.0	14.0	346.0	36098	GEO S/C (reorbited)
11	125.0	1000	15.0	42600	0.0030	0.0	270.0	90.0	36221	GEO S/C (reorbited)
12	375.0	3000	15.0	42600	0.0030	0.0	90.0	270.0	36221	GEO S/C (reorbited)

Table 3. List of all the simulated GEO fragmentations. The events listed in blue were simulated with SDM, those in red were simulated with DAMAGE.

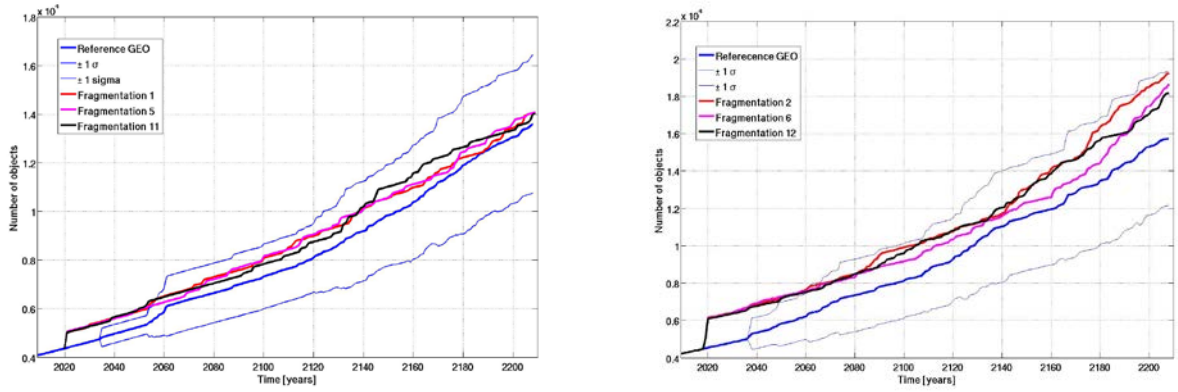

Figure 13. Left panel: Average number of object in the GEO region for the Reference scenario (thick blue line) compared with the cases number 1 (red line), number 5 (magenta line) and number 11 (black line) of Table 3 (see text for details). Right panel: Average number of object in the GEO region for the Reference scenario (thick blue line) compared with the cases number 2 (red line), number 6 (magenta line) and number 12 (black line) of Table 3(see text for details). The thin blue lines represent the ±1 σ intervals of the Monte Carlo runs.

2.1.4. Simulations: conclusions

The long term simulations of the LEO environment perturbed by the collisional fragmentation of large objects allowed us to highlight the main factors determining the environmental consequences associated with a given collision event.

First, as a general conclusion, it can be stated that, due to the highly stochastic evolution of the LEO environment, even the fragmentation of a massive spacecraft might not be able to alter the long term evolution of the LEO population beyond the intrinsic statistical variability associated with the Monte Carlo procedure.

On the other hand, thanks to the performed simulations, some parameters determining the long term effects of a fragmentation in LEO were identified. First the mass and the altitude of the event play a paramount role. It is actually a combination of these two factors, altitude and mass, that is driving the long term effects of a fragmentation in LEO. The orbital inclination is playing a minor role in this picture, with higher inclination targets slightly more prone to give rise to more visible long term effects.

The very large number of simulations performed certainly helped to add quantitative arguments to the a-priori intuitive hypothesis about the importance of mass and orbital altitude of the fragmented targets in the long term evolution of the LEO debris population.

The situation is different in the GEO region. The lower number of background objects and the reduced number of stochastic collisions (on average about 1.5 over 200 years) makes the growth of objects any additional fragmentation much more significant than in LEO. The addition of a massive fragmentation lives a signature on the environment that is detectable throughout the investigated time span. In the case of the GEO simulation the only factor important to assess the long term consequences of a fragmentation appears to be the mass of the target. Events happening in the GEO ring, or in inclined orbit at the GEO altitude (abandoned objects) or in a disposal orbit above the ring produce similar long term evolutions.
The evaluation norm described in the paper allows to highlight the differences between comparative long term evolution scenarios and offers a quantitative measure of the effects of specific parameters affecting the evolution.

3. The CONCEPT analytical model

A semi-analytical model, named CONCEPT, was developed with the aim of having a fast yet reliable software tool to estimate the criticality of user-defined objects, on the line of what discussed in Sec. 2.1.
CONCEPT makes use of a hybrid approach to evolve the LEO population, following a fragmentation event, and to estimate the criticality of user-defined objects. This hybrid approach utilises the capabilities of the DAMAGE evolutionary model to evolve the population of new fragments, whilst making use of stored population data (representing the contents of control volumes) and an empirical approach to induce a simple model of the collision probability in order to estimate the additional collision risk arising from new fragments. CONCEPT has been designed to operate as an interface between the user and the DAMAGE model, although no direct access to DAMAGE is provided. In this way, CONCEPT is able to overcome the limitations of the traditional "analytical" approach (namely, a focus on predictions of the mean number of objects and an inability to express the uncertainty/spread around the mean), and benefit from the advantages of a full evolutionary model, without incurring significant computational speed costs. In the tests reported here, CONCEPT was able to demonstrate a 20-times speed up over DAMAGE (ignoring the time taken to build the control volume database), whilst still being able to provide generally reliable estimates of criticality.
The details of the model are described in detail in the Final Report. Here we are showing a few results obtained applying CONCEPT to some of the fragmentations of Table 1, along with the comparison of the CONCEPT and DAMAGE output on the same scenario.

3.1. The probabilistic criticality norm

On the line of the C* norm defined in Sec. 2.1.2.3, the calculation of an addition evaluation metric based on a probabilistic approach has been included within the CONCEPT tool. The advantages of such a probabilistic approach are that the criticality metric is bounded between 0 and 1, can be readily understood and translated into text-based descriptors, and it can be used within a probabilistic framework that incorporates other probability-based metrics (e.g. the probability of the triggering fragmentation event occurring) through simple mathematical formulae.
The probabilistic criticality norm provides an evaluation of the probability that the number of objects in any Monte Carlo run in the fragmentation scenario is greater than the number of objects in any run in the reference scenario,

$$P_i = P[n_{FRAG}(i) > n_{REF}(i)] \tag{3.1}$$

such that

$$P^* = \frac{1}{N}\sum_{i=1}^{N} P_i = \frac{1}{N}\sum_{i=1}^{N} P[n_{FRAG}(i) > n_{REF}(i)] \tag{3.2}$$

Again, P^* can be evaluated over the number of years (or time-steps) in the simulation or the number of years (or time-steps) following the fragmentation event. P_i can be calculated by constructing the probability density functions $f(n_{FRAG}(i))$ and $f(n_{REF}(i))$ at every time-step using the number of objects observed in each Monte Carlo run for the fragmentation and reference scenarios. The probability that the number of objects in the fragmentation scenario is greater than the number of objects in the reference scenario is then

$$P_i = \int_0^{n_{FRAG}(i)} \left\{ f_{FRAG}(n_F) \int_0^{n_{REF}(i)} f_{REF}(n_R) dn_R \right\} dn_F \tag{3.3}$$

In practice, the probability density functions are not continuous: the outputs from CONCEPT represent the density functions as histograms with finite resolution. Consequently, the value of P_i is computed from the double summation,

$$P_i = \sum_{n_F=0}^{n_F=n_{FRAG}(i)} \left\{ P_{FRAG}[n_F] \sum_{n_R=0}^{n_R=n_{REF}(i)} P_{REF}[n_R] \right\} \tag{3.4}$$

where $P_{FRAG}[n_F]$ is the probability that a population in the range of $[n_F - \Delta n,\ n_F]$ objects will be found in the total debris population (i.e. background population plus new fragments arising from the criticality test), $P_{REF}[n_R]$ is the probability that a population in the range of $[n_R - \Delta n,\ n_R]$ objects will be found in the reference (background) population, and Δn is the resolution (or bin size) in the number of objects. In the prototype, Δn = 500 objects. The interpretation of the P^* (and P_i) values requires careful consideration. In particular, it is not immediately obvious that if the probability density functions $f(n_{FRAG}(i))$ and $f(n_{REF}(i))$ are identical then P_i will be 0.5 (Figure 14, left panel). If the expected value of $f(n_{FRAG}(i))$ is higher than the expected value of $f(n_{REF}(i))$ then P_i > 0.5 (Figure 14, right panel). Other factors, such as the bin resolution used to construct the probability density functions and the number of Monte Carlo runs, can influence the actual probability estimate, such that the actual output is not exactly 50% (Figure 15).

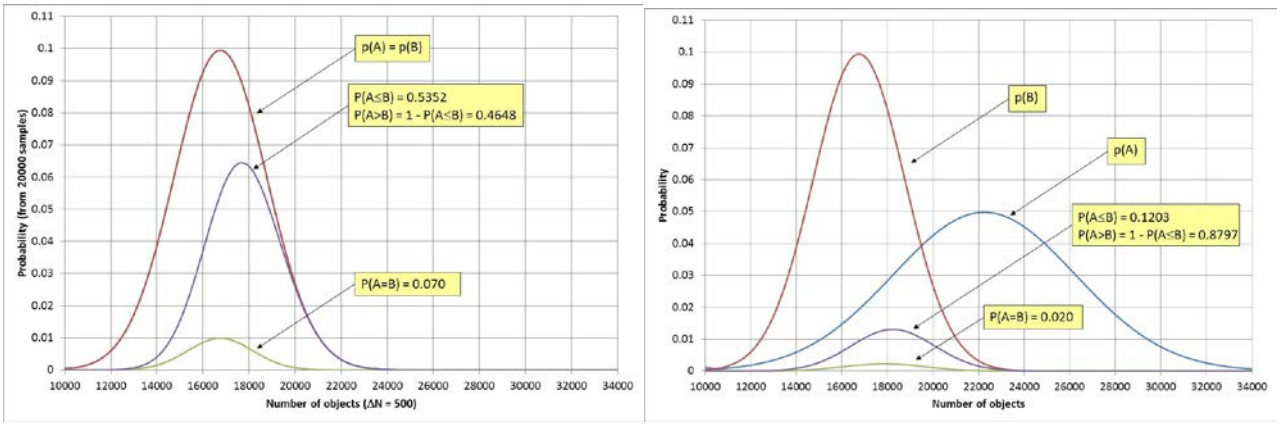

Figure 14. Left panel: . Two identical Gaussian probability distributions and the probability that a sample drawn from one distributions will be of equal value or greater than a sample drawn from the other distribution. Right panel: Two non-identical Gaussian probability distributions and the probability that a sample drawn from one distributions will be of equal value or greater than a sample drawn from the other distribution.

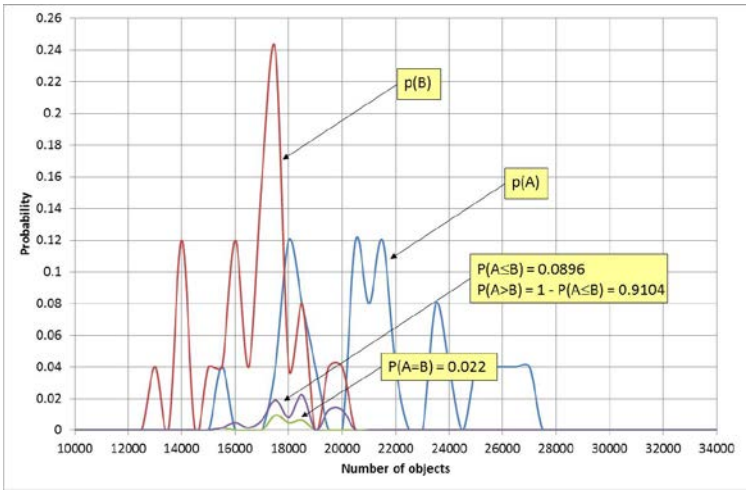

Figure 15. Two non-identical Gaussian probability distributions generated using 25 samples, and the probability that a sample drawn from one distributions will be of equal value or greater than a sample drawn from the other distribution.

The value of P_i, can be normalised to give a new criticality metric at each epoch,

$$\Delta P_i = \frac{P[n_{FRAG}(i) > n_{REF}(i)] - P[n_{REF}(i) > n_{REF}(i)]}{P[n_{REF}(i) > n_{REF}(i)]} \tag{3.5}$$

which describes the change in the probability with respect to the reference case, with the corresponding, average value over the full projection (or from the fragmentation epoch) given by

$$\Delta P^* = \frac{1}{N}\sum_{i=1}^{N} \Delta P_i \tag{3.6}$$

3.2. CONCEPT results

Table 4 lists the outputs of the criticality assessment of 24 cases, plus Envisat, for break-ups occurring in 2020. In addition, Table 4 provides the equivalent C^* criticality metric estimated using full DAMAGE simulations. The CONCEPT results for cases highlighted in yellow (1B, 8B, 15B, 23D and 25D) are shown in more detail later in this section.

The correlation between the DAMAGE and CONCEPT estimates of C^* for the 24 cases (excluding Envisat) in Table 4 was calculated to be $R^2 = 0.7324$ (Figure 16, left panel). Based on a linear fit between the two sets of values (gradient = 1.8805 and offset = 0.0155), CONCEPT appears to predict C^* values that are approximately twice those predicted by DAMAGE.

There is good agreement between the CONCEPT estimates of C^* and P^* for the 24 cases (excluding Envisat $R^2 = 0.9827$ for a quadratic fit) in Figure 16, right panel, and the CONCEPT estimates of P^* and ΔP^* ($R^2 = 0.9913$ for a power law fit) in Figure 17. These results demonstrate the consistency of the criticality metrics used within CONCEPT.

Case ID		Mass (kg)	INC (deg)	ALT (km)	Target Type	DAMAGE	CONCEPT		
						C*	C*	P*	ΔP* (%)
ENV		8050	98.2	759	Envisat	0.2784	0.4725	0.6102	12.12
1	B	3600	5	801	Ariane 5 R/B in GTO	0.0469	0.0262	0.5509	1.39
2	A	350	52	1414	Globalstar	0.0687	0.1423	0.5810	6.92
4	A	1500	63	800	Molniya	0.0007	0.0050	0.5447	0.26
6	A	1250	65	1500	US-K Oko	0.0687	0.0004	0.5435	0.04
7	B	1400	65.8	976	Cosmos-3M R/B	0.1105	0.4015	0.6425	18.20
8	B	8300	71	844	Zenit-2 R/B	0.6285	0.5818	0.6632	21.82
10	B	1400	74	771	Cosmos-3M R/B	0.0691	0.0658	0.5617	3.30
11	B	1400	74	985	Cosmos-3M R/B	0.3861	0.3818	0.6362	17.04
12	B	1400	74	1189	Cosmos-3M R/B	0.3510	0.5289	0.6737	24.01
13	A	1400	74	1586	Cosmos-3M R/B	0.1629	0.5573	0.6705	23.41
14	A	1750	81.2	601	Tselina-D	0.0335	0.0163	0.5483	0.85
15	B	2750	81.2	859	Meteor-2	0.1285	0.2906	0.6133	12.72
15	C	1340	81.2	853	Vostok R/B	0.0764	0.1387	0.5807	6.79
16	B	1410	82.5	948	Tsiklon-3 R/B	0.4323	0.6555	0.6503	19.64
17	B	1410	82.5	1236	Tsiklon-3 R/B	0.1636	0.7543	0.6786	24.9
19	B	1400	83	969	Cosmos-3M R/B	0.0968	0.3764	0.6298	15.85
20	B	1400	83	1190	Cosmos-3M R/B	0.2031	0.5239	0.6701	23.34
21	A	700	86.4	778	Iridium	0.0351	0.0305	0.5521	1.56
23	C	4000	98	675	Helios-2 in SSO	0.0244	0.0447	0.5537	1.78
23	D	8000	98	639	Zenit-2 R/B in SSO	0.0475	0.0628	0.5543	1.89
24	C	4000	98.5	780	SSO S/C	0.1569	0.2371	0.5961	9.57
25	A	1000	99	855	NOAA-19	0.0083	0.1166	0.5744	5.65
25	D	8000	99	997	Zenit-2 R/B in SSO	0.8475	2.2156	0.8744	60.89

Table 4. CONCEPT: Fragmentation by catastrophic collision (> 40 J/g) in 2020.

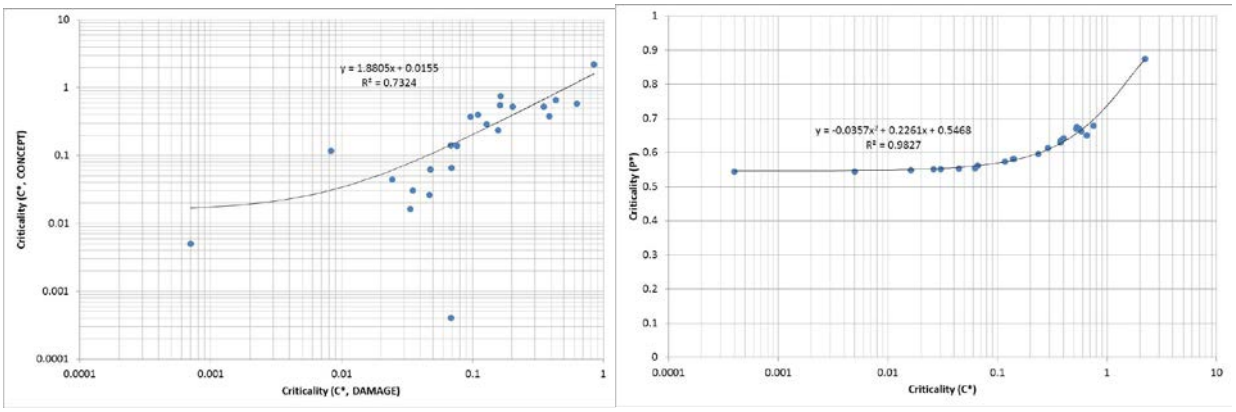

Figure 16. Left panel: Correlation between DAMAGE and CONCEPT estimates of the C* criticality metric for the 2020 fragmentation epoch. Right panel: Correlation between CONCEPT estimates of the C* and P* criticality metrics for the 2020 fragmentation epoch.

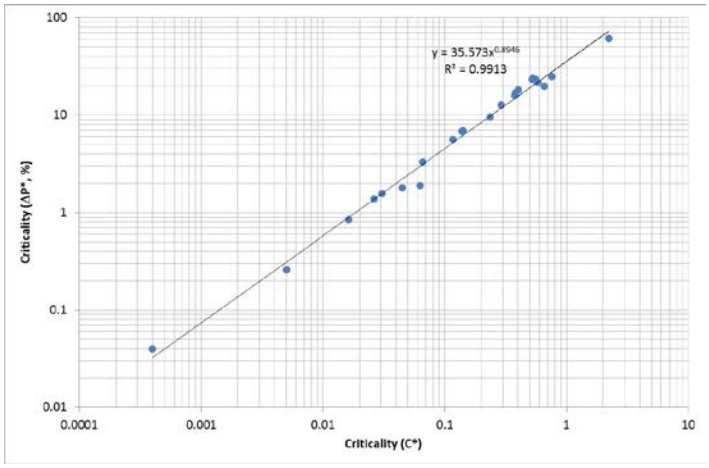

Figure 17. Correlation between CONCEPT estimates of the P* and ΔP* criticality metrics for the 2020 fragmentation epoch.

There was relatively weak correlation between the mass of the fragmentation object and the *ΔP** criticality metric ($R^2 = 0.1707$ for a quadratic fit in Figure 18.A), with high values of *ΔP** produced for objects with masses of approximately 1500 kg (Cosmos and Tsiklon R/Bs) and objects with masses of approximately 8000 kg (Zenit-2 R/B). In contrast, the inclination of the fragmentation object did not affect the object's criticality ($R^2 = 0.061$ for a linear fit with gradient = 0.1688 and offset = 0.1227 in Figure 18.B).

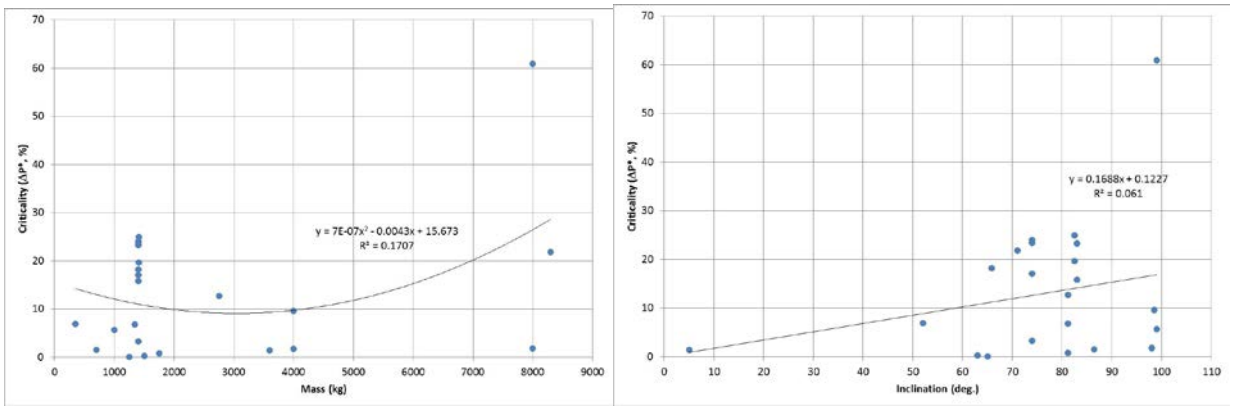

Figure 18. A) Correlation between object mass and CONCEPT estimates of the ΔP* criticality metric for the 2020 fragmentation epoch B) Correlation between object inclination and CONCEPT estimates of the ΔP* criticality metric for the 2020 fragmentation epoch.

Objects with larger orbits (larger semi-major axis) tended to be more critical than those with smaller orbits (Figure 19.A; $R^2 = 0.5076$ for a power law fit), although when the actual fragmentation altitude was examined (Figure 19.B), the correlation was weaker and *ΔP** values tended to be higher for fragmentation events at intermediate altitudes between 950 km and 1250 km ($R^2 = 0.3381$).

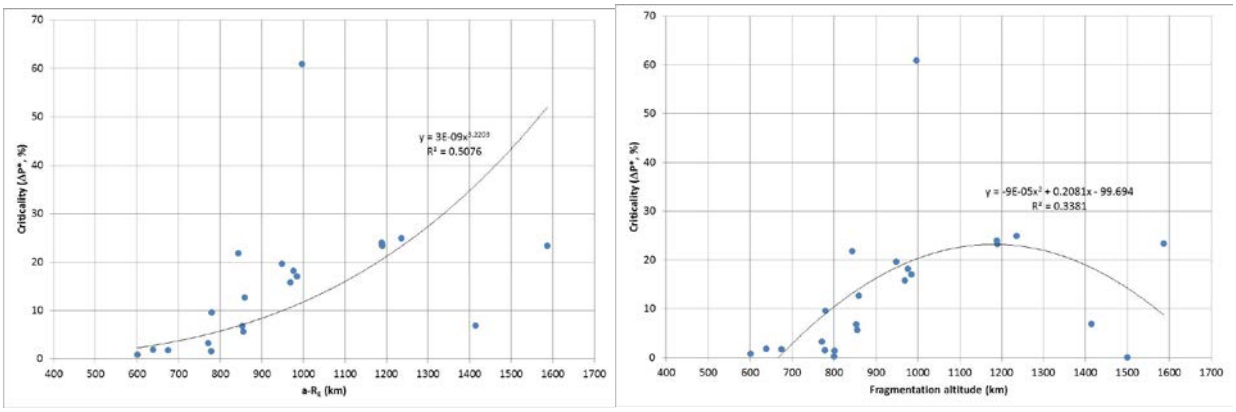

Figure 19. A) Correlation between object semi-major axis and CONCEPT estimates of the ΔP* criticality metric for the 2020 fragmentation epoch. B) Correlation between fragmentation altitude and CONCEPT estimates of the ΔP* criticality metric for the 2020 fragmentation epoch.

The partial dependence of the criticality identified by CONCEPT on the mass and the orbit semi-major axis/fragmentation altitude corresponds with the results observed in the SDM results for the full simulations, although some caution is needed: all of the object characteristics change between the 24 object cases and differences in the criticality may not always be attributed to one parameter.
To provide an illustration of the agreement between the results generated by CONCEPT and those produced by DAMAGE, five cases were selected from Table 4 and key parameters – the number of objects in LEO and the corresponding criticality metrics – were investigated. The average number of objects predicted by CONCEPT (and DAMAGE) for cases 1B, 8B, 15B, 23D and 25D and the 2020 fragmentation epoch are shown in Figure 20 -Figure 22. Following those results, Figure 23 -Figure 24 show the evolution of the criticality metrics for the same cases, with a comparison of the C_i metrics produced by DAMAGE and CONCEPT in Figure 23.
In all of the cases, except 25D, there is very good agreement between CONCEPT and DAMAGE. Case 25D is a Zenit-2 upper stage in a near-circular, Sun-synchronous orbit at an altitude of approximately 1000 km. In the DAMAGE results, the debris cloud produced by the fragmentation of this object are relatively long-lived but ultimately decay to leave the debris population unperturbed in the long-term. However, the CONCEPT results show that the fragmentation debris from the initial catastrophic collision of the Zenit-2 R/B is sufficient in number, and in an important orbital regime, to cause sustained collision activity. This resulted in an ever-increasing deviation away from the reference population in a way that resembles the Envisat validation case for the same epoch.

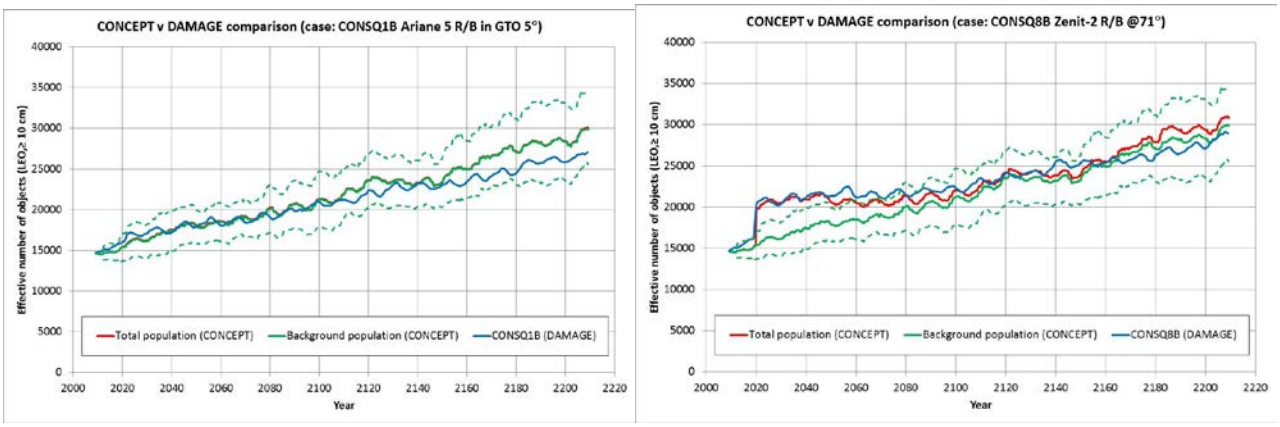

Figure 20. A) Comparison of the number of objects predicted by DAMAGE and CONCEPT for case 1B (Ariane 5 R/B in GTO) and fragmentation in 2020. The averages of 25 Monte Carlo runs and the standard deviation from the reference case are shown. B) Comparison of the number of objects predicted by DAMAGE and CONCEPT for case 8B (Zenit-2 R/B at 71°) and fragmentation in 2020. The averages of 25 Monte Carlo runs and the standard deviation from the reference case are shown.

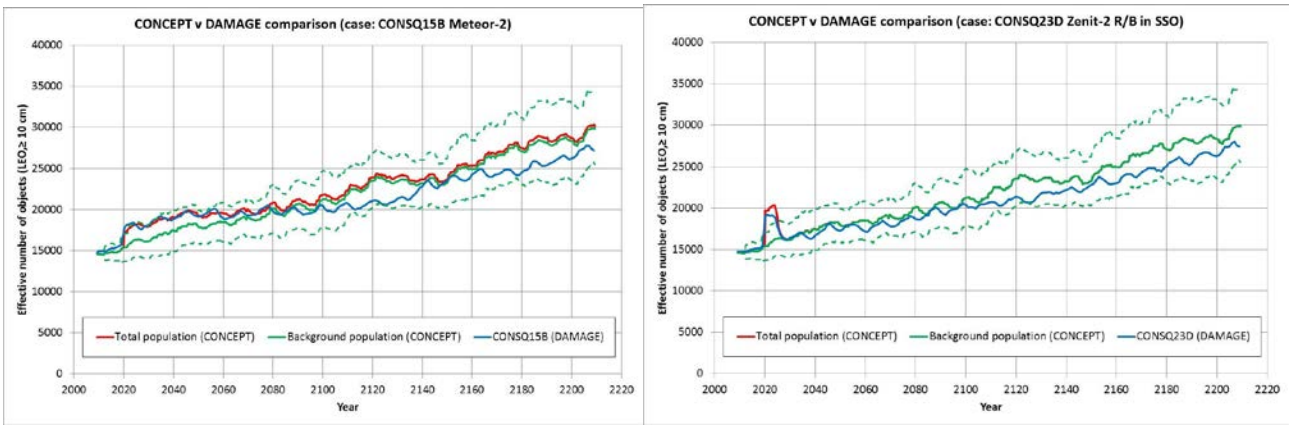

Figure 21. A) Comparison of the number of objects predicted by DAMAGE and CONCEPT for case 15B (Meteor-2) and fragmentation in 2020. The averages of 25 Monte Carlo runs and the standard deviation from the reference case are shown. B) Comparison of the number of objects predicted by DAMAGE and CONCEPT for case 23D (Zenit-2 R/B in Sun-synchronous orbit) and fragmentation in 2020. The averages of 25 Monte Carlo runs and the standard deviation from the reference case are shown.

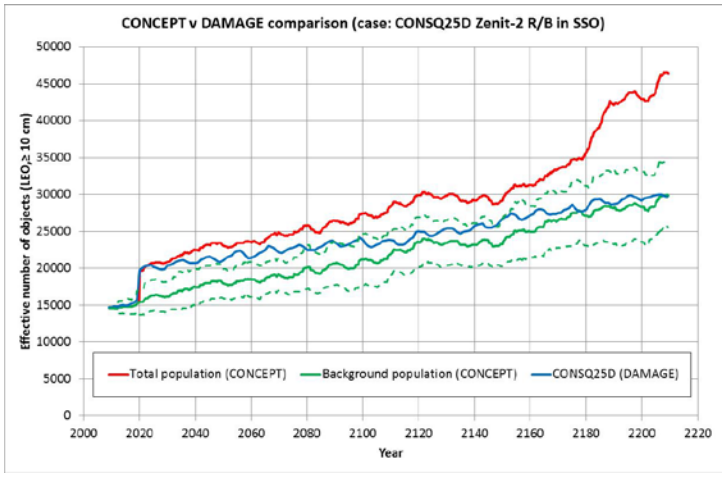

Figure 22. Comparison of the number of objects predicted by DAMAGE and CONCEPT for case 25D (Zenit-2 in Sun-synchronous orbit) and fragmentation in 2020. The averages of 25 Monte Carlo runs and the standard deviation from the reference case are shown.

Figure 23.A shows the evolution of the C_i criticality metric over the projection period for five cases (1B, 8B, 15B, 23D and 25D in Table 4) as computed by the full version of DAMAGE. In all of these cases, DAMAGE predicts that impact on the environment, with respect to the average population for the reference case, reduces relatively quickly to a value below 1 (i.e. within one standard deviation of the reference population) and demonstrates no real long-term effect. In the worst case – object 25D (Zenit-2 R/B in Sun-synchronous orbit) – the criticality remains close to a value of 1 throughout the projection period, but remains above this value only for the first 20 years following the fragmentation event.

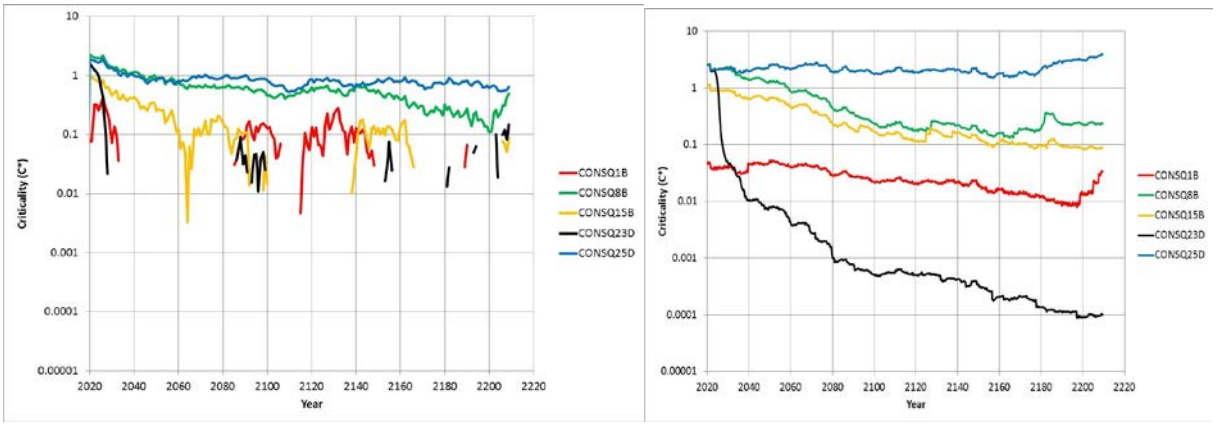

Figure 23. A) DAMAGE results showing the criticality metric C_i as a function of time for five cases with fragmentation in 2020. B) CONCEPT results showing the criticality metric C_i as a function of time for five cases with fragmentation in 2020.

The results from CONCEPT (Figure 23.B) for the C_i criticality metric are broadly similar to those computed by DAMAGE above. In particular, all cases except 25D have only a limited impact on the environment, with respect to the average population for the reference case and demonstrate no real long-term effect. The behaviour of the C_i metric computed by CONCEPT for object 25D does differ from the behaviour seen in the DAMAGE results, in that the criticality remains at a consistent level above a value of 1 throughout the projection period, with an increase after 2180 (which follows the behaviour seen in the number of objects).

Figure 24.A and B show the evolution of the P_i and ΔP_i criticality metrics for the five cases highlighted above. Here, the cases 1B (Ariane-5 R/B in GTO) and 23D (Zenit-2 R/B in Sun-synchronous orbit with fragmentation at 639 km altitude) show minimal impact on the population. For the former case, the effective number of fragments – i.e. the number of fragments weighted by the proportion of the orbit that is spent in LEO – is small and leads to the result seen. In the case of the Zenit-2 R/B, the number of fragments generated by the catastrophic collision is substantial but these decay quickly resulting, again, in a limited impact on the population. For cases 8B and 15B (Zenit-2 R/B at 71° and Meteor-2, respectively) the value of P_i remains elevated throughout the projection period but declines at a moderate rate such that the probability of a higher number of objects is approximately 65% after an interval of 60 years from the initial break-up and approximately 57% after an interval of 100 years. In contrast, the fragmentation of the Zenit-2 R/B at 1000 km results in a 90% probability of a higher number of objects after 60 years, and 85% after 100 years.

The difference in the probability, with respect to the reference case, is measured by the ΔP_i criticality metric in Figure 24.B. These results show some small residual effects of the GTO break-up (case 1B) that last for much of the projection period, which is contrasted by the substantial change introduced by the Zenit-2 R/B break-up in case 25D. Displaying the ΔP_i criticality metric in this way also enables a deeper understanding of the criticality, that is not offered by the use of a single average value (e.g. in Table 4). In particular, the time taken for the ΔP_i value to decay is of interest in these cases and one might consider an additional criticality metric based on this decay time. For example, the time taken for the ΔP_i value to decay to 10% of the reference case value was immediate for 1B, due to fewer fragments resident in LEO, and approximately 5 years for 23D, 60 years for 15B, and 100-130 years for 8B (the ΔP_i value did not decay to 10% for case 25D in the projection period). By this alternative metric, case 15B is 12 times worse than case 23D, and case 8B is about 20 times worse than case 23D.

An analysis of the fragmentation events of Table 4 in the epoch 2070 was performed too. The full results can be found in the Final Report.

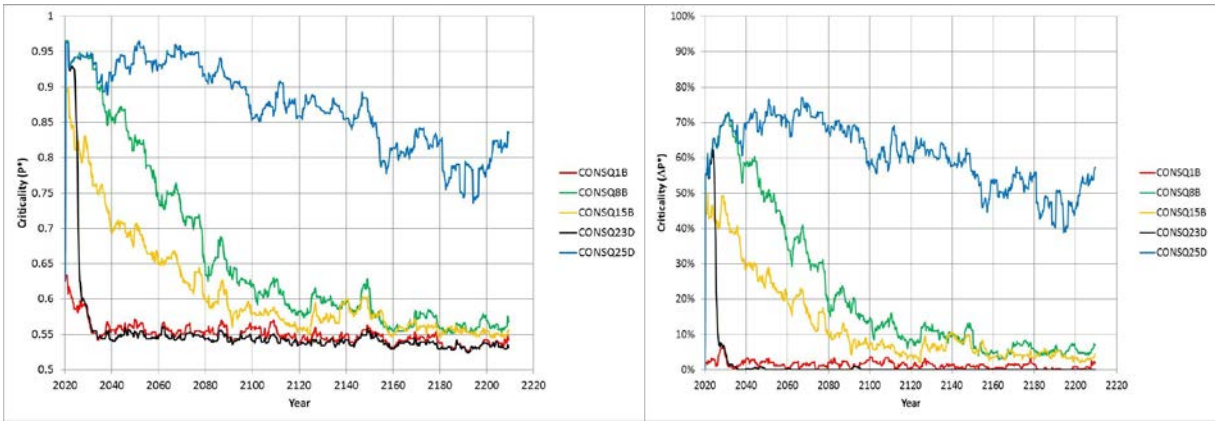

Figure 24. A) CONCEPT results showing the criticality metric P_i as a function of time for five cases with fragmentation in 2020. B) CONCEPT results showing the criticality metric ΔP_i as a function of time for five cases with fragmentation in 2020.

4. The ranking index

Exploiting the results of the simulations described in Sec. 2.1 a quantitative measure of the criticality of the artificial objects in LEO was devised. Such a measure is important under different aspects. It would be a measure of the perspective danger posed to the environment in case an object would become non-cooperative, and therefore could be used to rank active removal priorities. Moreover, it would help spacecraft operators in easily assessing the present collision risk faced by a given asset in space, and thus driving possible mitigation actions (e.g., disposal strategies).
Moreover, as is the case of the Palermo Scale [1] in the Near Earth Objects field, it could serve as a good mean to spread the public awareness of the danger posed by space debris by allowing a wider non-specialist audience to catch, with a single number, the environmental criticality of a given spacecraft.
Having these issues in mind, in this contract we invented the Criticality of Spacecraft Index (hereafter, CSI), an analytical tool, easy and swift to compute, which grabs the importance of the parameters identified by simulating selected fragmentations. The final goal is to measure the danger represented by typical classes of objects, in order to be able to rank the abandoned space objects in terms of the possible effects on the environment of the spacecraft and, conversely, in terms of the effect of the environment on the spacecraft itself.
The CSI applies in principle to abandoned objects (debris) since an active object, able to perform avoidance maneuvers, could theoretically avoid most of the collisions with debris larger than 10 cm if an efficient Space Surveillance network is in place. Moreover, the CSI is useful only for large objects; in fact, small, centimeter sized objects, although possibly very dangerous as projectiles, do not represent a threat to the environment at large if fragmented, since they would not generate large debris clouds. Given the expected usage of such an index, it should take into account the characteristics of the environment where the object moves, as well as the physical and orbital details of the objects itself. In our case the environment is considered in terms of the spatial density of objects, together with the residual lifetime in space, the mass and the inclination of the orbit. In the following subsections each one of these dependencies is discussed and detailed. Moreover, the CSI can be computed either for a specific epoch or as an average for a given interval of time.

4.1. The environment dependence

The environment is considered in terms of the spatial density of objects as a function of time and altitude. It is well known that the collision probability is higher in regions where a higher

concentration of objects is found. For this purpose, the spatial density of objects larger than 10 cm as a function of altitude, obtained from the Reference case described in Sec. 2.1.1 is considered.

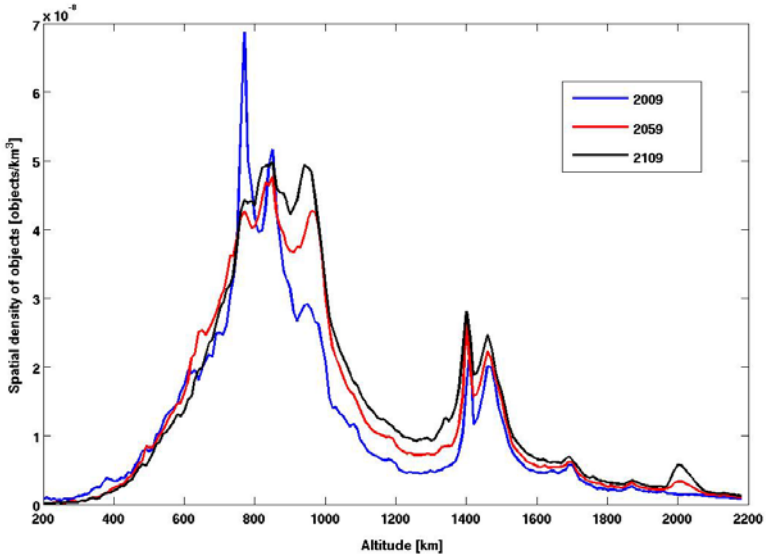

Figure 25. Spatial density of objects in the Reference scenario as a function of altitude in three different epochs: 2009 (blue line), 2059 (red line) and 2109 (black line).

In particular, for the Index computation, the resulting spatial density of objects as a function of altitude was recorded every year and stored.

As an example, Figure 25 shows the spatial density of objects larger than 10 cm as a function of altitude, for three different epochs.

The way in which the spatial density is taken into account in the CSI is as follows: given an epoch (or interval of time) and the orbital altitude, *h*, of the object under consideration, the spatial density, *D*, is taken from the stored values and normalized to the value of the maximal spatial density in the initial year 2009, that is the one at the altitude of 770 km, D_0. Therefore, the multiplicative contribution to the CSI accounting for the environment density is given by:

$$D(h)/D_0$$

4.2. Lifetime dependence

The danger represented by an object left in space and the probability that it will be destroyed by a collision is a function of the time that this object will spend in space. Moreover, as shown in 2.1.2.2 the long term consequences of a fragmentation are much more severe for events happening at high altitudes where the cleaning effects of the atmosphere are not effective. Therefore the residual lifetime of an object is an important parameter to include in the index computation.

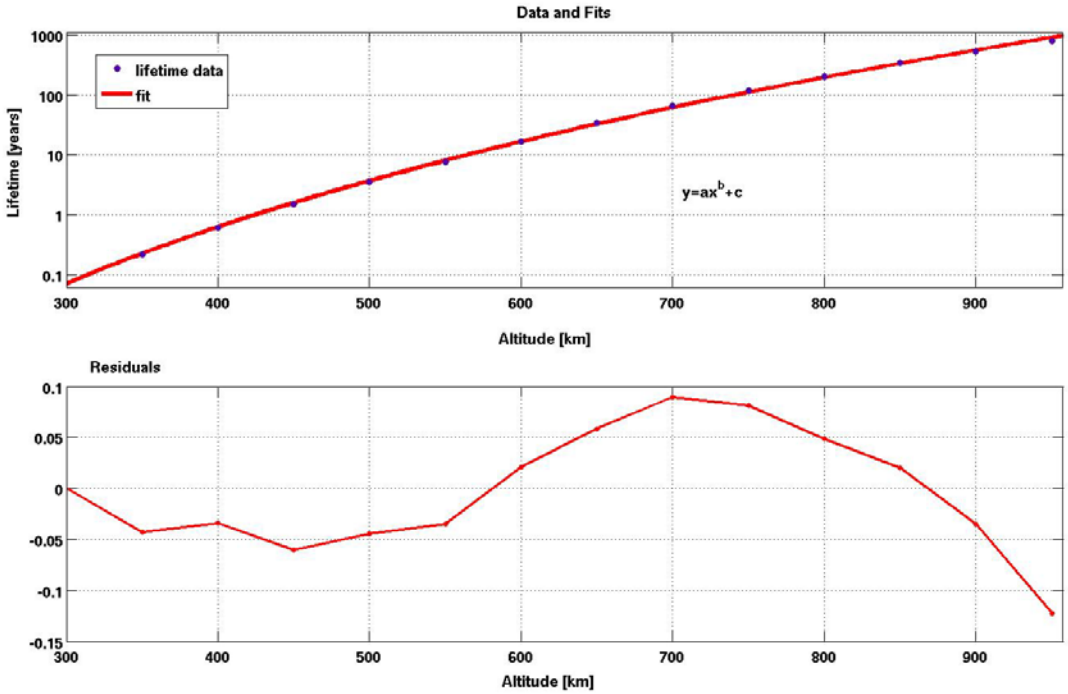

Figure 26. Orbital lifetime of a sample object with A/M = 0.012 m^2 kg^{-1} as a function of altitude. The upper panel shows a power law fit to the lifetime values and the bottom panel shows the residuals of the fit (see text for details).

The lifetime of the objects, as a function of the orbital altitude *h*, is estimated from an average lifetime given by the curve shown in Figure 26 computed assuming an area over mass ratio, A/M=0.012 m^2 kg^{-1}, which reflects the average value observed for intact objects. An average solar flux between 110 and 130 units is considered. The lifetime curve was computed as a power law fit of the form:

$$log(lifetime) = a\, h^b + c \qquad (4.1)$$

where a = 14.18, b = 0.1831 and c = −42.94 are the coefficients of the fit.
Therefore, given an object with mean altitude h (note that, for LEO objects having low eccentricity, the semimajor axis can be used as a good approximation of h), the CSI component accounting for the lifetime is given by:

$$life(h)/life(h_0)$$

where *life(h)* is computed with Eq. (4.1) and the normalizing value is computed, as a default, for h_0 = 1000 km.

4.3. Mass dependence

In Sec. 2.1.2 it clearly emerged that, along with the altitude of the event, the other most influential parameter in determining the environment consequences of a given fragmentation is the mass, *M*. This fact is taken into account in the index by including the term:

$$M/M_0$$

where the normalizing factor is arbitrarily taken as M_0=10000 kg. An alternative explored is to use the same exponent found in the NASA breakup model by expressing the mass term as:

$$(M/M_0)^{0.75}$$

It has been checked that the adoption of the 0.75 exponent does not change significantly the results. Therefore, for the sake of simplicity, in the following the value of the exponent used is 1.

4.4. Inclination dependence

It is well known that the collision risk is maximum for high inclination orbits that can cross all the other orbits in their range of altitude and that can lead to very high mutual inclinations (and therefore high impact velocities) due to the precessing orbital planes. For this reason an inclination (i) dependence is included in the CSI, in the form:

$$\frac{1 + k\,\Gamma(i)}{1 + k}$$

Where:

$$\Gamma = \frac{1 - \cos(i)}{2},$$

and k = 0.6 since the typical flux of debris on an almost equatorial orbit is about 60% of the flux on a polar orbit. Note that the Γ expression is devised in order to properly weight retrograde orbits, which would be under-weighted if a simple *sin(i)* term would be included.

4.5. Index definition

Combining the terms described above, the final definition of the CSI reads as:

$$\Xi = \frac{M(h)}{M_0}\frac{D(h)}{D_0}\frac{life(h)}{life(h_0)}\frac{1 + k\,\Gamma(i)}{1 + k}.$$

The definition was kept as simple as possible in order to allow its easy application and understanding by the largest possible community; the larger the value of the CSI, the more dangerous to the environment is an abandoned object. Note that, thanks to the normalization, for all the space objects in our population Ξ < 1. Note also that, in theory, it is not mathematically bound by 1 since, e.g., a hypothetical polar object exceeding 10 tons and orbiting around 1000 km of altitude could have Ξ> 1. In order to consider possible time variations in the environment, the CSI could also be computed taking into account the average density of objects over an interval of time (e.g., 10 years) instead of the single value in the year of reference.

4.6. Index application and ranking

The CSI corresponding to the year 2020 was computed for every LEO object with mass larger than 100 kg listed in the MASTER 2009 population. Table 5 lists the first 15 objects having the largest values of the CSI in our population.

It is worth stressing that, at this stage, the purpose of the current study is not to compile a ranking of catalogued objects, pointing out which one is the most dangerous; rather, our goal here is to describe the CSI and show its potential applications. Therefore in our rankings presented below we will not list names of objects, but only physical and orbital characteristics. This will allow to identify families of objects particularly dangerous for the environment and prone to perspective active debris missions.

As the only notable exception, we identify the top object in Table 5 as a Zenit 2 upper stage, due to its distinct characteristic well known to the professionals in the field.

As it can be noticed, all the objects have large mass, well above one metric ton. However, it is also worth noting that the ranking is not just dominated by the mass, given that the semimajor axis (i.e., the mean altitude) plays a significant role, and that all the objects in the table have high inclinations.

Figures 27 - 28 graphically show the distribution of the CSI values, N, as a function of different orbital and physical parameters for the highest 100 values obtained. In all the figures it can be noticed how all the highest index colors pertain to large objects, above a few metric tons.

Moreover, all the top CSI values have perigee above about 600 km of altitude. The situation is less marked for the inclination distribution. Most of the massive objects have inclination larger than 50 degrees and, within this sample of large spacecraft, again the top CSI values pertain to high inclination orbits, as expected.

In Figure 28 the objects appear as circles with diameters proportional to their mass. It is worth noting how the orbital distributions obtained in the right panel of Figure 28 compare nicely with Fig. 13 of [10] where the orbital distribution of the existing LEO R/Bs and S/Cs having highest mass and collision probability products (computed with 100 Monte Carlo runs of LEGEND) is shown.

	a [km]	e	i [deg]	Mass [kg]	Ξ
1	**7372.2**	**0.002**	**99.25**	**9000.0**	**0.313**
2	7365.7	0.003	64.98	4500.0	0.163
3	7343.1	0.003	64.99	4955.0	0.161
4	7342.1	0.004	65.04	4955.0	0.160
5	7355.2	0.006	64.49	4500.0	0.154
6	346.5	0.007	65.28	4500.0	0.151
7	7342.9	0.006	64.95	4500.0	0.146
8	7349.3	0.005	64.81	4500.0	0.145
9	7332.1	0.005	64.98	4955.0	0.143
10	**7222.0**	**0.001**	**71.00**	**9000.0**	**0.139**
11	**7221.6**	**0.000**	**70.98**	**9000.0**	**0.139**
12	7336.6	0.004	64.70	4500.0	0.135
13	**7227.3**	**0.002**	**70.88**	**8226.0**	**0.135**
14	7335.5	0.006	64.86	4500.0	0.134
15	7333.3	0.009	65.08	4500.0	0.131

Table 5. List of the 15 objects having the largest values of the CSI in our MASTER 2009 population. Objects in boldface are upper stages, the others are satellites.

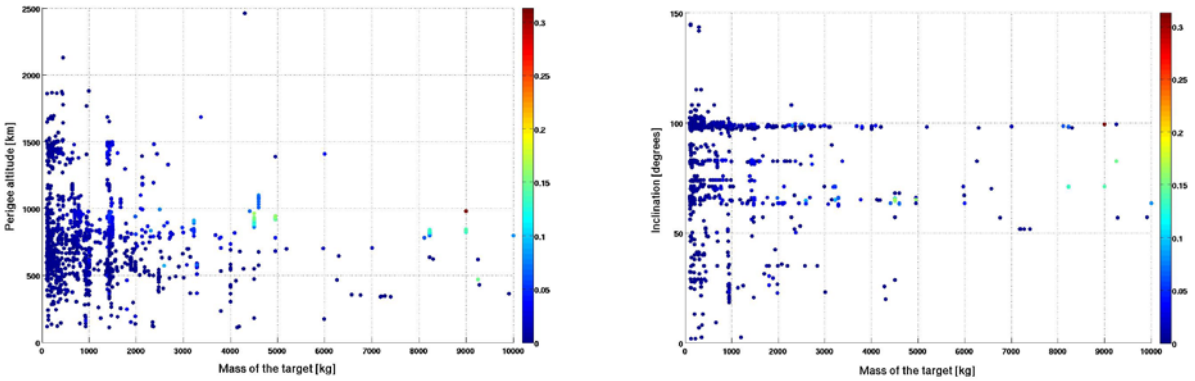

Figure 27. Left panel: The highest 100 values of Ξ in the perigee altitude vs. mass plane; the color of the points is coded according to the value of Ξ, as shown by the color bar. Right panel: The highest 100 values of Ξ in the inclination vs. mass plane; the color of the points is coded according to the value of Ξ, as shown by the color bar.

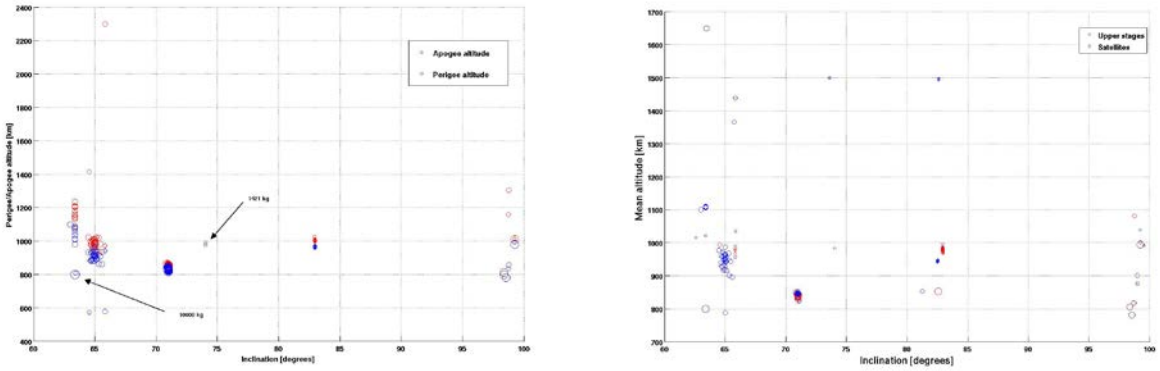

Figure 28. Left panel: Distribution of the first 100 objects in the Ξ ranking as a function of inclination and perigee (blue circles) and apogee (red circles). Note that each object is represented by two circles, one blue, for the perigee, and one red, for the apogee. The size of the circles is proportional to the mass of the object. Right panel: Distribution of the first 100 objects in the Ξ ranking as a function of inclination and mean altitude. The blue circles relates to satellites while the red ones relate to upper stages. The size of the circles is proportional to the mass of the object

This is a further confirmation that the CSI can be considered as a reliable indicator of the actual risk faced and posed by objects in LEO and as such is a good analytic, fast and easy-to-compute proxy for active removal strategies planning.
Moreover, it is interesting to note that Figure 28 points out that the majority of the top 100 values of CSI is composed by satellites, rather than by rocket bodies.

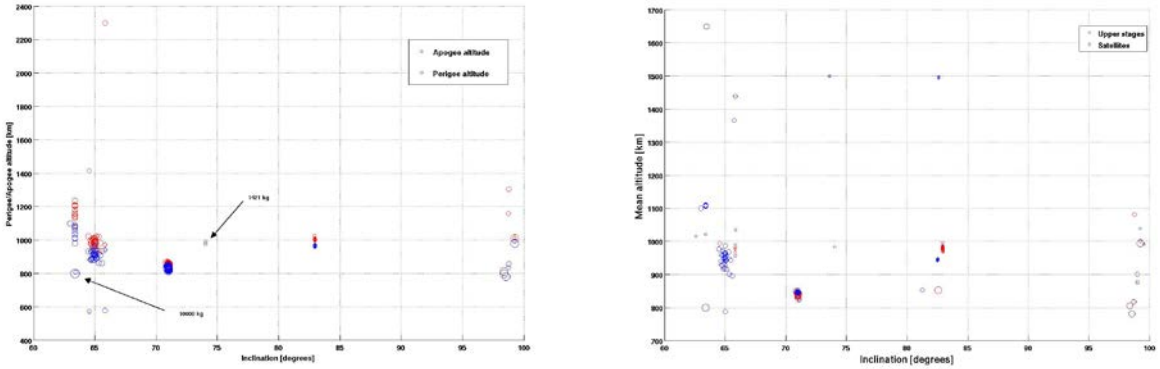

Figure 29. Left panel: Distribution of the first 100 objects in the Ξ ranking as a function of inclination and perigee (blue circles) and apogee (red circles). Note that each object is represented by two circles, one blue, for the perigee, and one red, for the apogee. The size of the circles is proportional to the mass of the object. Right panel: Distribution of the first 100 objects in the Ξ ranking as a function of inclination and mean altitude. The blue circles relates to satellites while the red ones relate to upper stages. The size of the circles is proportional to the mass of the object

The CSI index devised in this Contract is a simple, fast, easy-to-compute analytic tool able to rank the abandoned space objects in term of the danger they can pose to the environment (or, conversely, in terms of the risk they face from the environment) taking into account their orbital and physical characteristics. It has been shown how it is able to catch the main known features of the in-orbit collision risk and that it can be viewed as a good proxy for active debris removal planning.

5. Contract conclusions and future work

The main results of the Contract can be summarized as follows:

- A first quantitative, physical estimation of the long term effects of a specific fragmentations in Earth orbit was given, allowing a classification of the fragmentation events in term of the physical and dynamical characteristics of the targets;
- Two novel evaluation metrics were proposed to visualize and quantify the effects of a fragmentation on the evolution of the debris population and, in general, to evaluate the impact of different simulation scenarios on the long term evolution;
- A semi-analytical space debris environment long term evolution model (CONCEPT) was developed allowing quick, though accurate, simulations;
- An analytical index able to rank the abandoned space objects in term of the danger they can pose to the environment (or, conversely, in terms of the risk they face from the environment).

In the Contract work a huge amount of simulations were performed, generation output data in excess of 1 TB. This *treasure trove* including, for every simulated scenario, number of objects, characteristics of all the collisions, record of all the orbital crossing (all vs. all) registered within CUBE algorithm, etc, can certainly be exploited in the future for further analysis that might be devised.

In this respect, a number of future improvements on the results described in this document can be hypothesized. E.g., building on the experience gained in this work, it would be desirable, in future studies, to concentrate on a smaller number of highly significant events (mass larger than ~ 1000 kg and altitude above ~ 800 km) with a number of MC runs in excess of 100. Concerning the ranking index, the validity of the CSI as a prioritization ranking for active debris removal targets could be further tested by implementing it in the long term evolution codes, e.g., SDM 4.2. Thus the long term evolutions of the environment obtained using the CSI and those obtained using the standard parameter (*mass x collision probability*) could be compared. Finally a way to incorporate long term evolution uncertainties – both “formal uncertainties” from the Monte Carlo averaging and “systematic” modeling uncertainties (i.e., upper and lower ranges of evolutions due to parameters choice in the physical models such as solar flux, atmospheric density, fragmentation threshold, . . .) – into the index computations (e.g., in the yearly density terms) could be explored.

6. References

[1] Chesley S.R., Chodas P.W., Milani A., Valsecchi G.B. and Yeomans D.K., Quantifying the risk posed by potential Earth impacts, *Icarus*, 159, 423- 432, 2002.

[2] Liou J.-C., An active debris removal parametric study for LEO environment remediation, *Advances in Space Research*, 47, 1865-1876, 2001.

[3] Liou, J.C., Rossi, A., Krag, H., Xavier James Raj, M., Anilkumar, A.K., Hanada, T., and Lewis, H., Stability of the Future LEO Environment, Action Item 27.1, Working Group 2, Inter-Agency Space Debris coordination Committee, IADC-12-08, October 2012.